Deep electrical structure over the Paleoproterozoic intracratonic Kaladgi rift basin in southwestern India imaged from magnetotelluric studies

Amit Kumar [a,*], Danda Nagarjuna [a,b], M. Santosh [c,d], S.K. Begum [e], C.K. Rao [a]

[a] *Indian Institute of Geomagnetism, New Panvel, Navi Mumbai 410218, India*
[b] *Department of Geosciences, College of Science, United Arab Emirates University, Al–Ain 15551, Abu Dhabi, United Arab Emirates*
[c] *School of Earth Sciences and Resources, China University of Geoscience Beijing, Beijing 100083, China*
[d] *School of Physics, Chemistry and Earth Science, University of Adelaide, Adelaide SA 5005, Australia*
[e] *Department of Geophysics, Andhra University, Visakhapatnam 530003, India*

A R T I C L E   I N F O

A B S T R A C T

The disintegration of the Columbia supercontinent during the late Paleoproterozoic generated major rift basins in the constituent continental fragments. The Kaladgi basin, located between the southern part of the Deccan volcanic province (DVP) and the northern part of the Dharwar craton, is a Columbia rift-related basin in southwestern India that preserves a complex history from initial fault-controlled mechanical subsidence during rifting, thermal subsidence along a collision zone, crustal thinning due to stretching and erosion associated with doming. The Paleoproterozoic basins worldwide show higher uranium concentration and many deposits are also established in the Purana basins of India. In the present study, the lithotectonic architecture of this basin using broadband magnetotelluric (∼320 Hz–3000 s) soundings in the western segment of the Kaladgi rift basin along two profiles. Two-dimensional (2-D) inversion of data using a 2-D nonlinear conjugate gradient algorithm along both profiles provides insights into the deeper structure of the basin. Our results reveal a thin sheet of Deccan volcanic, sedimentary successions belonging to the Badami and Bagalkot groups, and Proterozoic sediments from top to bottom beneath this basin. The crustal structure is highly heterogeneous and associated with deep-seated faults, and its thickness increases from the eastern Dharwar craton (∼30 km) to the western Dharwar craton (∼45 km). The crustal conductors are interpreted as mafic intrusions derived from the underplated basalts. The moderate conductive features may correspond to carbonate fluids trapped within the faults/fractures zone during basin initiation. The conductive features in the lower crust and the Moho are interpreted as fluids derived from underplated intrusions through plume impact. The NNW trending Chitradurga Suture Zone (CSZ) signature and the Bababudan-Nallur Shear (BNS) in the crust and upper mantle depth are imaged along both MT profiles. This study provides insights into the lithology and tectonic architecture of a long-lived rift basin involved in multiple tectonic events from the late Paleoproterozoic to the late Cretaceous.

1. Introduction

The Columbia supercontinent is considered the Earth's oldest coherent and closely packed assembly of continental fragments into a united landmass (Rogers and Santosh, 2002; Nance et al., 2014; Meert and Santosh, 2017). The rifting and disintegration of Columbia during the late Paleoproterozoic led to diverse magmatism processes, and sizeable intracratonic rift basins in the constituent continents witnessed prolonged sedimentation (Rogers and Santosh, 2004). In Peninsular India, these Paleoproterozoic rift basins are popularly termed 'Purana Basins' (Purana meaning ancient) and include the Vindhyan, Chattisgarh, Khariar, Indravati, Pranhita-Godavri, Cuddapah, Kaladgi, and Bhima. Rifts can form in many plate-tectonic settings, including intracratonic zones related to continental collision, transtensional rifts along transform faults, complex plate interactions at subduction zones, and transform margins. The Archean cratons were formed by the collision and accretion of individual continental nuclei (Radhakrishna and Naqvi, 1986). Convergence of East Antarctica

and Indian craton along Eastern Ghat mobile belt occurred at ∼1.9 Ga. The collision between the Bhandara–Bastar and Dharwar craton and Satpura and Aravali–Delhi mobile belts is broadly defined as Proterozoic events (Mishra, 2011). Orogenic activity associated with rifting may deform rifts and convert them into complex basins. The rifting of Columbia possibly involved a superplume activity (Santosh et al., 2009) during ∼1.9–1.8 Ga and was also marked by oxygenation of the atmosphere and ocean (Chu et al., 2007), and the formation of giant radiating dyke swarms and orogenic belts during ∼1.85–1.75 Ga (Hou et al., 2008; French et al., 2008; Shellnutt et al., 2018; Santosh et al., 2018), seawater was rich in carbonate before 1.8 Ga (Ohmoto et al., 2004), whereas sulfate was more abundant after that period (Poulton et al., 2004; Johnston et al., 2006). The Vindhyan, Cuddapah, and Pranhita-Godavri basins are associated with thermal subsidence and contain Paleoproterozoic carbonate-rich sediments (Mishra, 2011). Mukherjee et al. (2016) inferred that the Kaladgi rift basin opened during the Columbia breakup, and carbonate-rich sediments of the basin indicate Paleoproterozoic rifting (Saha et al., 2016). The northward migration of the Indian plate over the Reunion hot spot produced massive tholeiitic basalts through fissures eruption that covered vast areas during the Cretaceous-Tertiary period (Gautam, 2001; O'Neill et al., 2003). In these regions, Archean tectonic boundaries are poorly defined (Peucat et al., 2013). Thus, complex tectonics might have formed the Kaladgi rift basin, including initial fault-controlled mechanical subsidence during rifting, thermal subsidence along the collision zone, crust thinning due to stretching, and erosion during doming activity.

In previous work, Vasanthi and Mallick (2006) analyzed gravity data inferring the Kaladgi Basin's northward extension under the Deccan basalts, and the thickness of the basin was estimated to be between 500 and 3500 m. Anand et al. (2016) conducted ground magnetic studies in the Chikotra River in the peripheral regions of the Deccan volcanic province (DVP) and the Kaladgi rift basin. They inferred that the Deccan basaltic flows (∼285 m) overlie the Proterozoic sediments (∼900 m thickness) that reside on an Archean basement. Using a heliborne transient electromagnetic study, Sridhar et al. (2017) inferred that the thickness of the Deccan traps in this basin is between 20 and 350 m. A high-resolution aeromagnetic study concluded that the magnetic anomalies in the Kaladgi rift basin are related to the significant structural trends, crystalline basement, lineaments, intra-basinal fault systems, half-graben structures, and concealed granitic plutons (Sridhar et al., 2018). The signatures of the Chitradurga boundary shear, Wajrakarur fault zone and other lineaments were inferred from regional aeromagnetic data (Anand and Rajaram, 2002; Rajaram and Anand, 2014; Rajaram et al., 2016). Based on gravity data, Ramadass et al. (2004) revealed the Bababudan-Nallur Shear and Chitradurga boundary thrust zones. The crust-mantle boundary (Moho) in the Dharwar craton around the study region is inferred to be at a depth range of 33–45 km through receiver function analysis (Gupta et al., 2003; Sarkar et al., 2003; Jagadeesh and Rai, 2008; Borah et al., 2014; Singh et al., 2015), satellite gravity studies (Vasanthi and Santosh, 2021). The Chitradurga shear zone marks the crustal tectonic boundary between the Chitradurga schist belt and Closepet granite (Chardon et al., 2008), which is uncertain in the trap-covered regions.

In this study, we used the Magnetotelluric (MT) technique to image the subsurface features beneath the western segment of the Kaladgi rift basin. In previous studies, the MT technique has successfully been utilized to image the sediment thickness, basement configuration (Danda and Rao, 2019), Sub basaltic imaging (Patro and Sarma, 2007; Patro et al., 2015), Archean suture zones, and lithospheric thickness in the different areas (Gokarn et al., 2004; Naganjaneyulu and Santosh, 2010a, 2010b, 2012; Abdul Azeez et al., 2015; Danda et al., 2017, 2023;

Pratap et al., 2018, 2023; Malleswari et al., 2019; Kusham et al., 2021a, 2021b). Significant inconsistencies among various techniques has resulted in poorly known geophysical properties at great depths within the Kaladgi rift basin. However, the comprehensive information on the crust and upper mantle structures beneath the Kaladgi rift basin is not well-imaged and inferred. In this study, we investigate the basin and lithosphere structure along two MT profiles to understand the deep tectonics and evolution processes of the Kaladgi rift basin and neighbouring regions.

2. Geology and tectonics

The north-south trending Closepet granites separate the Dharwar craton into western Dharwar craton (WDC) and eastern Dharwar craton (EDC), as shown in Fig. 1a. The WDC comprises tonalite gneisses older than 3.0 Ga (Taylor et al., 1984; Meen et al., 1992), 2.8–2.6 Ga greenstone belts of Dharwar Supergroup (Kumar et al., 1996; Nutman et al., 1996) in the northern part and 2.61 Ga potassic plutons, characterized by the melting of a depleted lower crust (Taylor et al., 1984; Jayananda et al., 2006). The EDC comprises 2.7–2.55 Ga regional tonalite gneisses and greenstone belts (Balakrishnan et al., 1999; Krogstad et al., 1991; Peucat et al., 1993; Chadwick et al., 2000; Rogers et al., 2007), and huge 2.56–2.50 Ga calc-alkaline to potassic (Closepet granites) plutonic bodies (Nutman et al., 1996; Jayananda et al., 2000). The EDC is subdivided into two domains based on thermal events that occurred earlier than 2.5 Ga (Jayananda et al., 2013, 2020; Gao and Santosh, 2020). The Archean suture is characterized by a steep mylonitic shear zone between the Chitradurga schist belt and the Kushtagi-Hungund greenstone belts in the northern part of the Dharwar craton (Jayananda et al., 2011, 2013, 2020). The Closepet granites were emplaced along the shear zone associated with the Chitradurga schist belt (Jayananda et al., 2000). The Dharwar Supergroup was deposited unconformably over gneisses and granites in the WDC (Chadwick et al., 1981). Granites and gneisses in the EDC cover volcanic greenstone belts with limited dimensions on all sides (Naqvi et al., 2006). The Paleoproterozoic convergence/collision, orogenic belts, and carbonate-rich sediments are correlated to rifting (Mishra, 2011), and giant radiating dyke swarms have also been reported from the Dharwar craton (Hou et al., 2008).

The DVP covers the western section of the east-west trending Kaladgi rift basin in the north, northwest, and southwest margins (Fig. 1b). The DVP rocks are basalts (rich in tholeiitic type with a minor amount of carbonate and mafic alkaline rocks) produced by a high degree of melting at a depth range greater than other flood basalts (Sen, 2001). The Badami and Bagalkot groups belong to the Kaladgi Supergroup, separated by erosional surfaces representing an angular unconformity (Jayaprakash et al., 1987). The Badami group sediments are almost undeformed and thin (Jayaprakash, 2007), whereas the Bagalkot group sediments are deformed, thick and show plunging anticlines, synclines, and steeply dipping faults. The younger Badami group sediments overlie older Bagalkot Group sediments and the crystalline basement. The Badami group rocks are distributed in the western and southern segments of the basin and consist mainly of horizontally dipping arenite, shale, and conglomerate (Jayaprakash, 2007). The Bagalkot group is further divided into two subgroups, which are separated by disconformity: the Simikeri subgroup, which is restricted to the east and central segments hosting felsic and mafic intrusives (dyke swarms), and a thick sequence of the Lokapur subgroup distributed throughout the basin and composed of quartzite, argillite, shale and carbonate facies (Jayaprakash, 2007). The Archean crystalline rocks (gneisses, greenstone belts and granites) form the basement of the Kaladgi supergroup. Toward the south of the western Kaladgi rift basin, the Chitradurga group
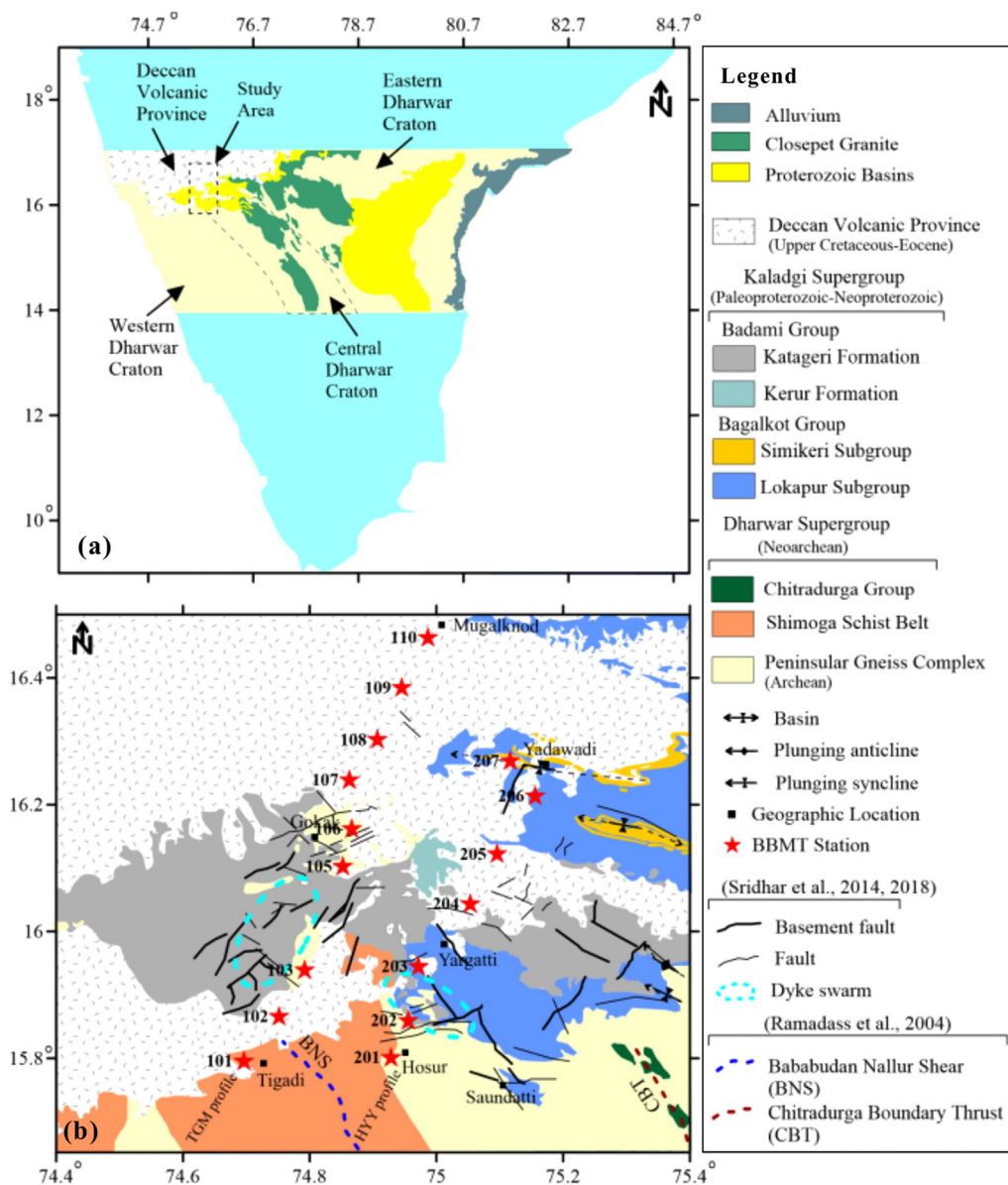
Fig. 1. (a) The geological map of the study area and its adjoining regions, (b) BBMT stations are located in the western section of the Kaladgi rift basin (modified after Mukherjee et al., 2016).

rocks occur as inliers with limited dimensions and comprise phyllites, quartz-chlorite schist, and amphibolite (Jayaprakash, 2007). In contrast, the older Bababudan group rocks are greywackes and conglomerates (Chadwick et al., 1985), and the peninsular gneissic complex dominated by tonalite-trondhjemite-granodiorite rocks (Jayaprakash, 2007).

3. Data acquisition and analysis

Broadband magnetotelluric data was acquired between 74°40′ E-75°10′ E and 15°48′ N-16°30′ N coordinate frame around 47 L/16 topo sheet frame located in the Karnataka state in southwestern India under the R&D program of the Indian Institute of Geomagnetism. All stations are located along two SW-NE trending profiles (Fig. 1b), the ∼80 km long Tigadi-Gokak-Mugalknod (TGM) profile holds 9 stations, and the ∼60 km long Hosur-Yargatti-Yadawsd (HYY) profile has 7 stations. The data were acquired using two sets of instruments, namely, MTU-5A V-5 system (Phoenix Geophysics, Canada) and ADU05 system (M/s Metronix, Germany) for

a period range of 0.003–3000 s and 0.01–1000 s, respectively with an interstation spacing of ∼9–13 km. Robust single-station estimates processed (using SSMT 2000 software, robust reference cascade decimation technique according to Jones and Jodicke (1984); Jones et al. (1989); PROCMT User' guide (1990)) the observed time series from electric and magnetic fields. The data quality is conditioned by the location of the stations, and good quality data were observed along the HYY profile. In contrast, noise affects the time series from the TGM profile at fewer stations. The bad segments of the time series containing spikes and trends were removed before frequency domain conversion. The phase response at a few stations is highly contaminated by cultural noise; those station's responses, including apparent resistivity, were discarded from data analysis.

The local near-surface inhomogeneities inherent in the MT data affect the dimensionality and directionality of the subsurface of the Earth (Ledo et al., 1998, 2002). The higher dimensional structure and inconsistent strike direction may also occur along the profile and depth if distortion factors are period-dependent (Ledo et al., 1998). The most effective distortion is 'galvanic', wherein electric
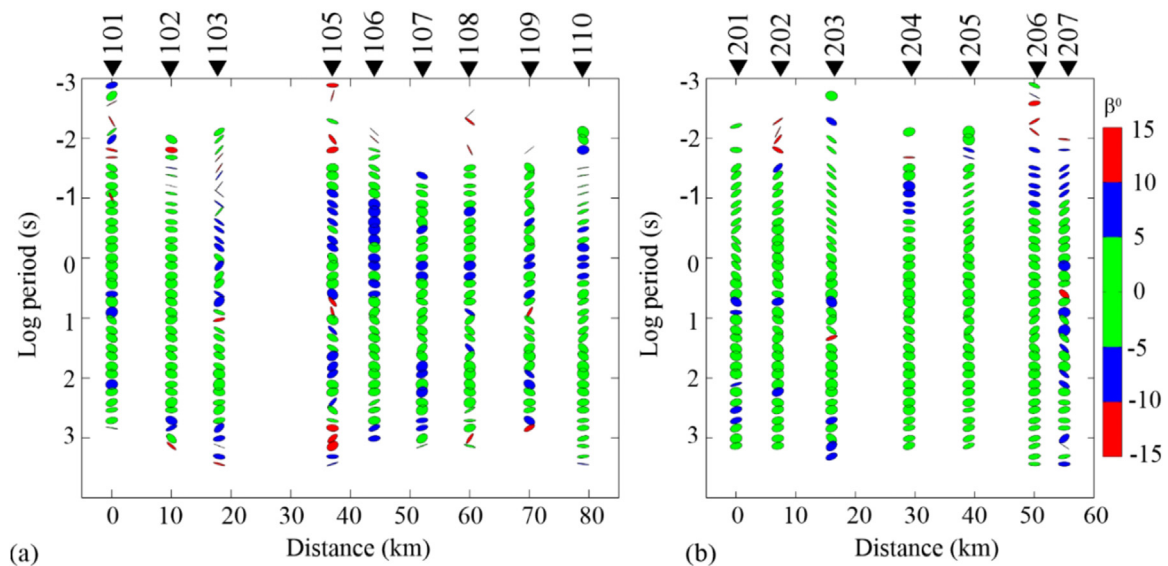
Fig. 2. The phase tensor analysis responses show a skew angle 'β' between $\pm 5°$ at most stations, (a) along the TGM profile and (b) along the HYY profile.

charge build-up on near-surface inhomogeneities modifies the regional conductive structures (Bahr, 1988; Jiracek, 1990), whereas inductive distortion is negligible (West and Edwards, 1985). The Phase tensor analysis is used to estimate the dimensionality of the subsurface, and it calculates phase-sensitive skew angle (β), maximum phase (Φ_{max}), minimum phase (Φ_{min}), and a directional angle (α) without any prior assumptions on the dimensionality of regional structure (Caldwell et al., 2004). The skew angle (β) is zero for an identical 2-D structure with a strike direction towards the Φ_{max} or Φ_{min}. The skew values within the range of $\pm 5°$ indicate a 2-D structure (Liang et al., 2018; Padilha et al., 2019; Danda et al., 2021, 2023) and otherwise a 3-D structure. Most sites show a skew angle of $<5°$, except in some stations at a few periods (Fig. 2a, b). It may be due to data quality, which indicates that the 3-D effects are generally localized at sites 105, 106, 206 and 207.

The approach of McNeice and Jones (2001) was applied for distortion correction and to define regional strike direction along both profiles. This is the extension of the Groom-Bailey tensor decomposition concept (Groom and Bailey, 1989), in which a global minimum is sought to determine the most appropriate strike direction and telluric distortion parameters for a range of periods and a set of stations. The regional strike estimation is usually problematic in case of more prominent telluric distortion (Jones and Groom, 1993). Thus, distortion parameters (shear and twist) were constrained first to estimate the stabilized strike response over the broadest band of periods. The shear and twist angles are less than $\pm 15°$ at all stations, except two stations from the HYY profile where the shear angle is $+30°$. However, overall, shear and twist angles lie within the limit of the normal range. The strike angles observed in the period range 0.1–1000s for all stations are shown by Rose diagrams (Fig. 3a and b); consistency in regional geoelectric strike angle is marked around N55°W (after correcting for 90° ambiguity) along both profiles. The tensor data are further decomposed for multi-stations multi-period bands; distortion parameters best fit most stations with RMS misfits less than 2 (Fig. 3c and d), which approximate 2-D structure along both profiles. The consistent strikes from each station in the single-period band are shown in Supplementary Data, Fig. S1. Consequently, we conclude that, on the whole, the dimensionality of the present profiles is quasi-2D for the crust and upper mantle, and 2-D inversion procedures apply to our data.

Subsequently, data from both profiles were fitted to a frequency-independent distortion model with a regional strike an-

gle of N55°W to obtain the scaled 2-D apparent resistivity and impedance phase responses (Fig. 4). Therefore, we assigned xy, yx components to the transverse electric (TE) mode (electric currents flow parallel to the geoelectric strike) and transverse magnetic (TM) modes (electric currents flow perpendicular to the geoelectric strike), respectively. The Niblett-Bostick depth approximation (Jones, 1983) is used to estimate the depth of electromagnetic field penetration. The penetration depth along both profiles for transverse electric and transverse magnetic modes responses are shown in Supplementary Data, Fig. S2.

4. 2-D inversion

The non-linear conjugate gradient (NLCG) inversion algorithm of Rodi and Mackie (2001) was used for 2-D inversion. The 2-D Earth models were discretized into 50×150 rectangular cells for both profiles. In which each cell is assigned conductivity values to fit the measured data. Thus, joint TE- and TM-modes responses were modelled for both profiles. The regularization parameter 'tau' is used to minimize the objective function, which is the sum of data misfit and the smoothness of the model. For both profiles, $\tau = 10$ was set for 2-D inversion according to the L-curve (Hansen, 1998), as shown in Supplementary Data, Fig. S3. The apparent resistivity and phase error floors were set to 10% and 5% for each mode in both profiles, except the TE mode of the TGM profile, which was set to 30% and 10%, respectively. The 2-D inversion was carried out by taking 100 Ω-m uniform half-space and also tried with 10 Ω-m and 1000 Ω-m half spaces by keeping the remaining parameters unchanged to understand the initial model effects. The resulting models from 10 Ω-m and 1000 Ω-m half-spaces produced structures similar to the 100 Ω-m half-space model. The Pseudo-sections illustrate a good match between the observed (Groom-Bailey decomposed and rotated) and modelled response along both profiles (Fig. 5a and b). The static shift coefficients were estimated from the inversion algorithm. Finally, 2-D inverted models (TGM and HYY models) from joint inversion of TE- and TM-modes responses were produced after 132 iterations with an RMS misfit of 1.66 along the TGM profile and 166 iterations with an RMS misfit of 1.94 along the HYY profile (Fig. 6). The fitting between each station's observed and modelled response curves are shown in Supplementary Data, Fig. S4.

The robustness of inverted models was tested by linear sensitivity analysis along both profiles, representing the slight change
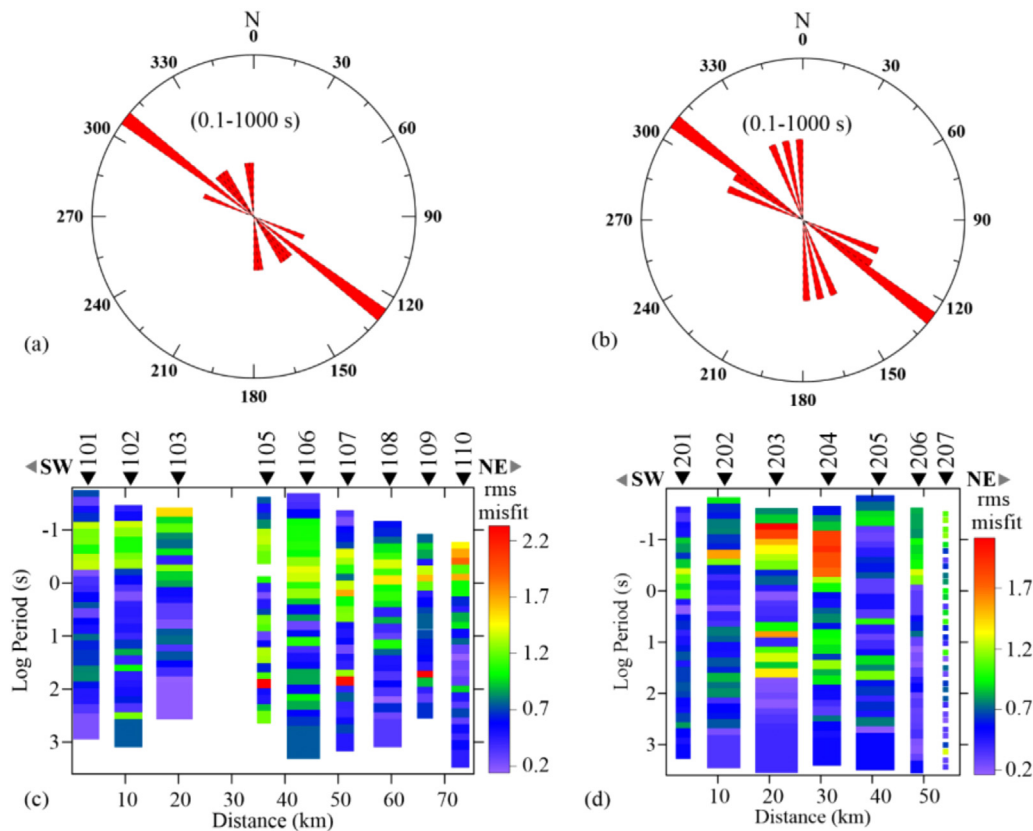
Fig. 3. Rose diagrams show regional geoelectric strike angle consistency at N55°W in the period range 0.1–1000 s (a, b), and RMS misfits obtained via multi-station, multi-period tensor decomposition (c, d), (left) along the TGM profile and (right) along the HYY profile.

in logarithm resistivity of observed data and model. The structure with sensitivity matrix values ≥0.0001 is considered a resolved feature (Brasse et al., 2002; Ledo et al., 2004; Naganjaneyulu et al., 2010; Danda et al., 2020). The TGM and HYY models show sensitivity values ≥0.0001, shown in Supplementary Data, Fig. S5. Where conductive features are supported by the high sensitivity value, C1, C2 and C3 lie in the 1–0.001, C5 lies in the 100–1, and C4 and C6 lie in the range of 10–0.01. These conductive features are tested for robustness by masking the conductive features with the 500 Ω-m resistive blocks and re-inverted the model, and after a few iterations, these conductive features reproduced in the model. In addition, a non-linear sensitivity analysis was conducted for each conductive feature. The forward response was calculated by masking the conductive feature with 2000 Ω-m resistivity while keeping other structures unchanged. This analysis was performed for all conductive features in the models independently. Supplementary Data, Fig. S6 shows the modeled and altered responses. The modified model responses show significant misfits compared to the original inversion models and infer that these features are robust. Based on these sensitivity test results, 2-D inverted models are fixed for ∼100 km depth to explain the Earth's subsurface structures along both profiles.

5. Interpretation and discussion

The electrical models produced from the TGM and HYY profiles within ∼20 km away in the western section of the Kaladgi rift basin display almost similar subsurface structures (Fig. 6). The TGM model shows destitute resistivity contrast compared to the HYY model. Highly conductive to moderate resistivity features in the HYY model and conductive features in the moderate resistive crust in the TGM model separate these models. The Chitradurga

Suture Zone (CSZ) and Bababudan-Nallur shear (BNS) boundary are revealed in the TGM model, while the HYY model shows only CSZ with resistivity contrast. This suggests that the deep tectonic features of the Kaladgi rift basin highly influence the crustal structure beneath these profiles.

5.1. Basin structure

The basement electrical structures of the Kaladgi rift basin along the TGM and HYY profiles are shown in Fig. 7. Proterozoic sediments with resistivity ∼100–2000 Ω-m and thickness ∼500–1000 m is deposited over resistive (>2000 Ω-m) crystalline basements with layers, where the resistivity of sediments increases with depth. These layers show flat, undulating shapes along the TGM and HYY profiles. Therefore, those in the fault/fracture zones are characterized by the Bagalkot Group sediments along the HYY profile. Flat-layer deposits are marked by the Badami Group sediments along the TGM profile. These shallow structure sediments are separated into two resistivity ranges; the Deccan basalts are explained with a resistivity of less than 100 Ω-m, and Proterozoic depositions are presented with a resistivity of ∼100–2000 Ω-m. The thickness of Deccan basalts and Proterozoic sediments are revealed at ∼285 and ∼900 m in the Chikotra River Basin (Anand et al., 2016), respectively. Airborne transient electromagnetic studies in the western section of the Kaladgi rift basin approximate the DVP thickness in a depth range of ∼20 m to 350 m (Sridhar et al., 2017). Deccan basalts thickness and resistivity value in the Kurduvadi gravity low were assessed ∼500–690 m with resistivity in the range of ∼30–60 Ω-m (Kailasam et al., 1976; Gokarn et al., 1992). Patro and Sarma (2007) revealed ∼200 m thick Deccan basalts with resistivity in the ∼30–100 Ω-m range. These findings possibly support Deccan basalts resistivity along both profiles. Deccan
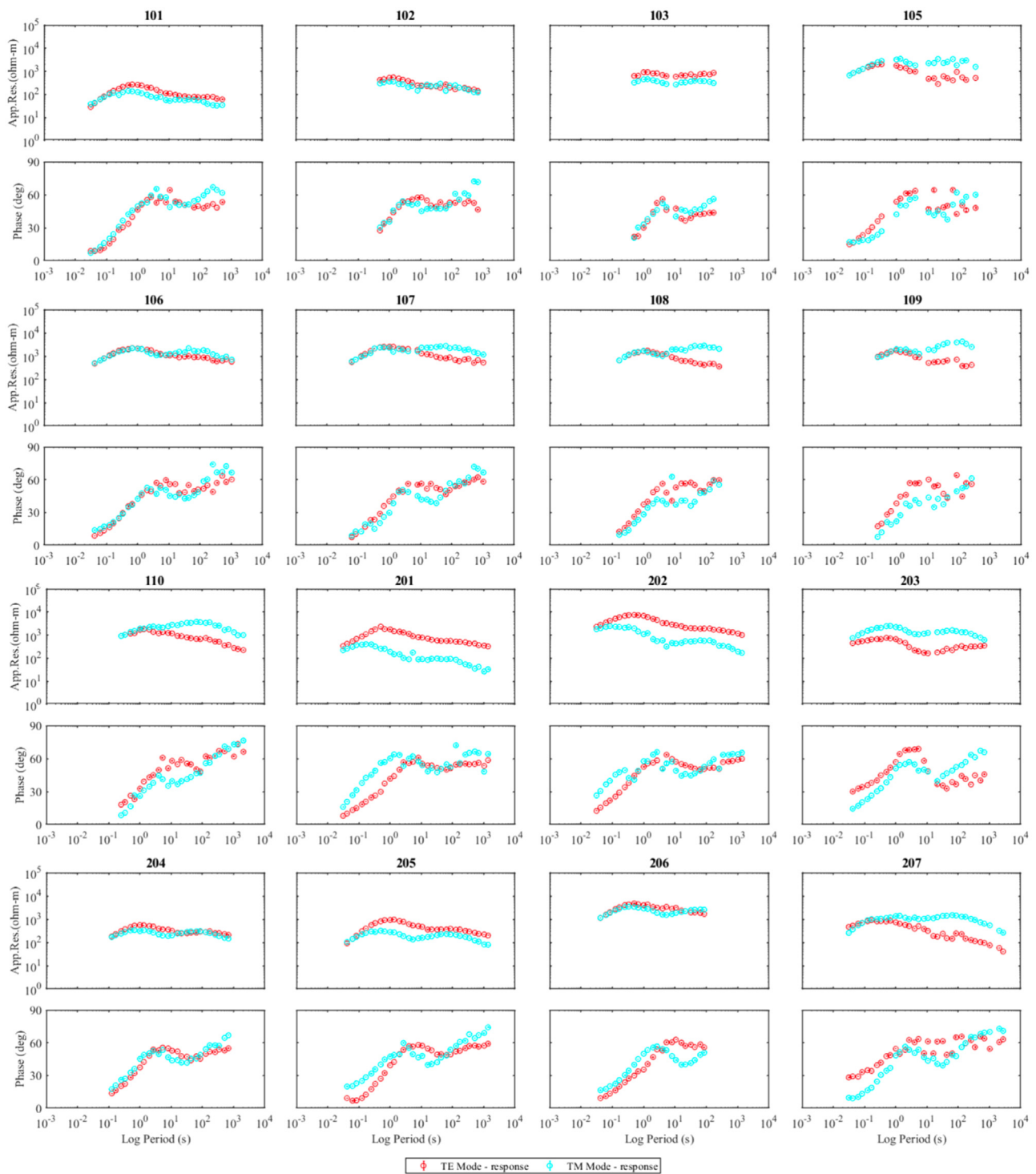
Fig. 4. Groom-Bailey decomposed and rotated apparent resistivity and phase response curves of TE- and TM-modes of all stations along the profile.

basalts are ∼100 m thick beneath stations 106–110 and very narrow beneath stations 204–205.

The Kaladgi sediments are interpreted with resistivity ∼100–700 Ω-m, where fault/fracture zones comprise deposits with resistivity in the range ∼700–2000 Ω-m along both profiles, which may support the different ages of sediments deposited in the basin as reported by Saha et al. (2016) and Joy et al. (2018). The moderate resistive sediments in the fractured zones indicate that the relic of crystalline rocks deposited after attrition and trapped carbonate fluids may cause moderate resistivity. The basin contains a cycle

of orthoquartzite-argillite-carbonates (Kale and Phansalkar, 1991). The Saundatti quartzites are coarse to fine-grained and deposited vertically to horizontally, reflecting the intensity of deformation (Jayaprakash, 2007). They also contain clay, micaceous, silica, and ferruginous material. The Yargatti argillite overlies dolomite with organosedimentary characters, consisting of silty to fine sandy clasts and argillaceous limestone. The Yadawadi limestones show silica and calcium content. Thick arenite rocks contain wonderful sand, silt, clay, silica and ferruginous material, in addition to the shale and laterite of the Badami Group. Thus, the amalgamation of
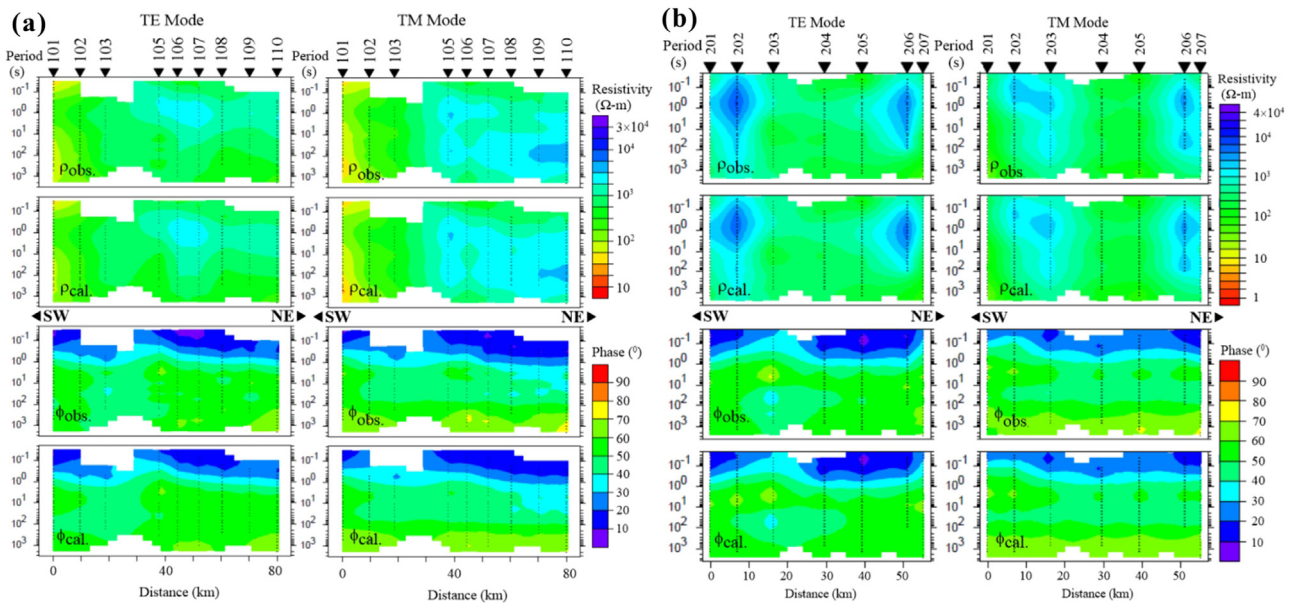
Fig. 5. Groom-Bailey decomposed and rotated (obs.) and modelled (cal.) apparent resistivity and phase pseudo-sections in the transverse electric and transverse magnetic modes for the TGM profile (a) and HYY profile (b). The triangles indicate the location of the sites, and the dots over the pseudo-section indicate the data points used in the period range at each site.
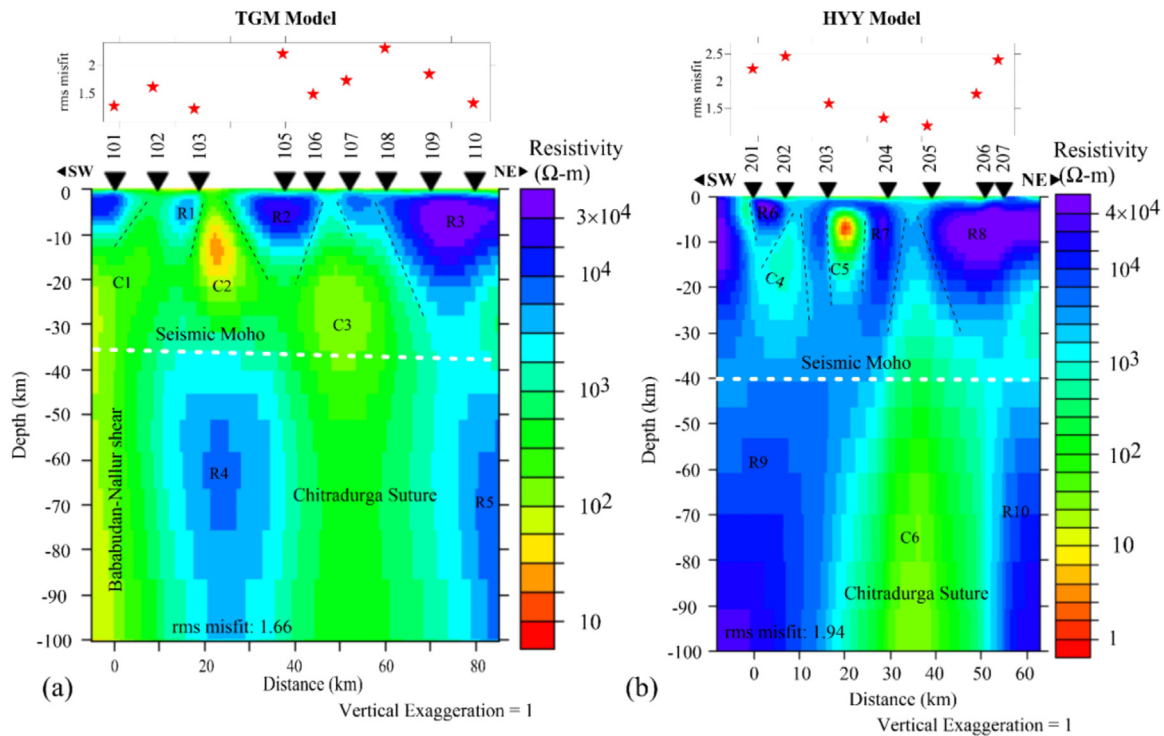

Fig. 6. Crust and lithospheric-mantle electrical structure from joint transverse electric and transverse magnetic modes 2-D inversion (with vertical exaggeration = 1) along the TGM and HYY profiles. RMS misfit value at each station plotted on top.

such composition might be the reason for the low resistivity nature of the Kaladgi rift basin sediments.

Two conductive (∼10–30 Ω-m) patches are identified beneath stations 102–103 and 203–204. Patro and Sarma (2007) revealed subtrappean Mesozoic sediments (∼10–20 Ω-m) between the Deccan basalts (∼30–100 Ω-m) and crystalline basement (∼3000 Ω-m) towards Kurduvadi gravity low. Kailasam et al. (1976) and Gokarn et al. (1992) findings from Kurduvadi gravity low indicate no signature of Mesozoic sediments. The MT estimates average thickness, whereas the profound electric resistivity studies are more sensitive to the local variation in thickness. The conductivity sediments are infrequent between the Deccan basalts and crystalline basements. Since the large station spacing between 102–103 and 203–204 sites, the inferences about the ∼200 m thick conductive patches at shallow depth may not be well resolved. Nevertheless, significant resistivity contrast at the shallow depth and known geology and geophysical observations perhaps corroborate such conductive patches in the MT data. However, better constraining the top conductive sedimentary patches within 1 km alone by using MT may require close station spacing MT observations.
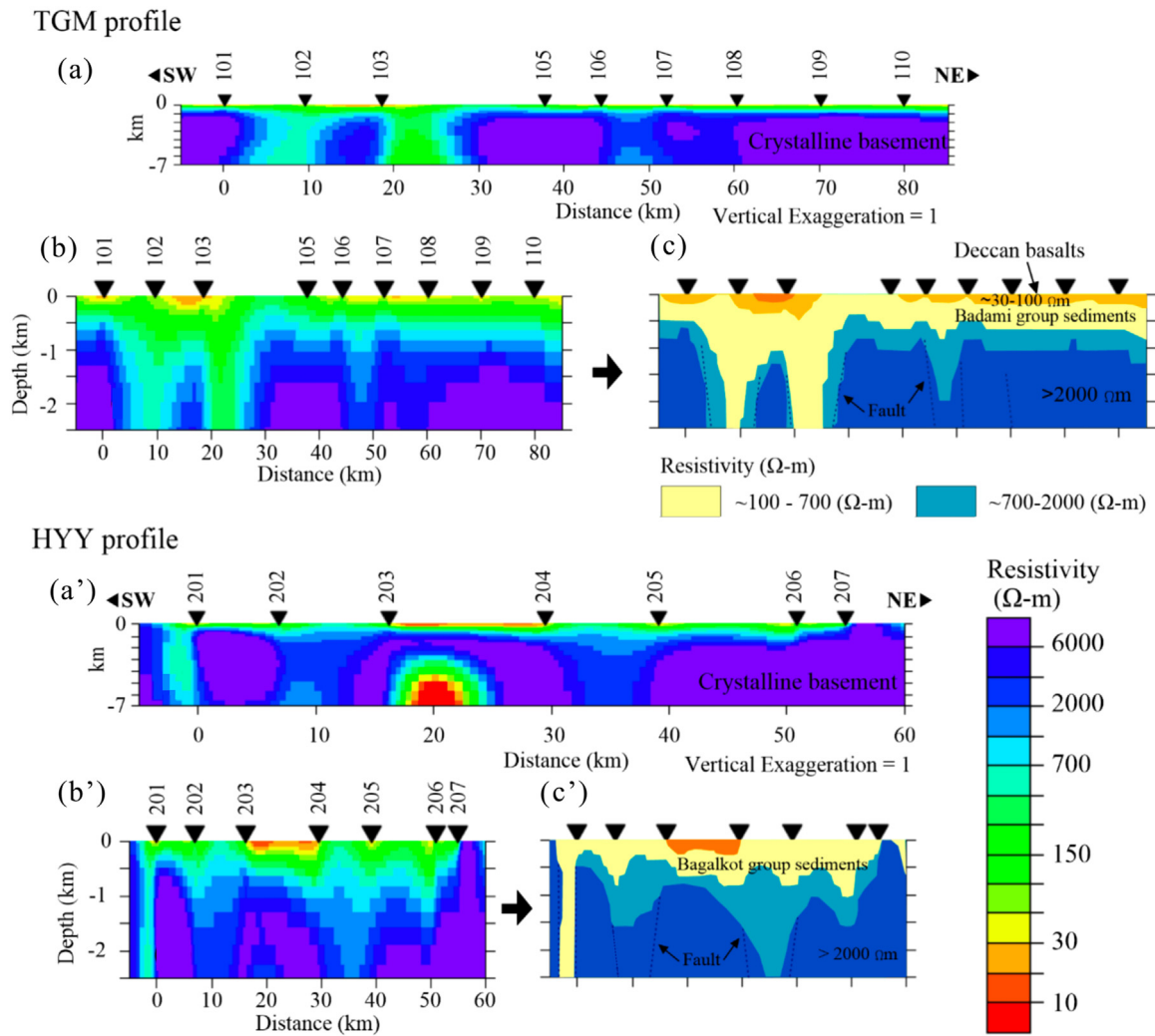
Fig. 7. The electrical structures of the Kaladgi rift basin. (a, a') Indicate Deccan basalts and Proterozoic sediments overlie crystalline basements, (b, b') Indicate Badami Group and Bagalkot Group sediments beneath the TGM and HYY profiles, respectively. (c, c') Cartoon sketches of the structure evident thickness and resistivity of Deccan basalts and Proterozoic sediments.

The surface conductivity may be due to rock compositions or flood basalts. The Deccan basalts towards the east are identified in the range ~30–100 Ω-m, as discussed above, while towards the west, the basalts are thick (~2500 m) and vary in the range ~10–200 Ω-m (Gokarn et al., 2003). Towards the southwest of the TGM profile, ~350 m thick low-resistive (conglomerate) sediments are identified with an intermediate high-resistive (quartz arenite) layer that underlies ~40 m wide Deccan basalts (Sridhar et al., 2017). The Badami group feldspathic arenites and shale units, carbonate rocks with kankar (Jayaprakash, 2007), and uranium mineralization were identified within the Badami arenites (Shobhita et al., 2011; Sridhar et al., 2014), which possibly explains the conductivity beneath the stations 102–103. Stations 203–204 are located over thick argillite and thin dolomite sequences; argillite contains mudstones, shales, and argillaceous limestone. The local enrichment in iron content has contributed to the development of hematite ore bodies and led to the formation of ferruginous laterite (Jayaprakash, 2007), which may cause conductivity.

5.2. Crustal structure

The MT stations are primarily located in basaltic flow-covered regions along the TGM profile, while fewer are along the HYY profile. Therefore, electrical structures up to 40 km depth are used to understand the crustal structure, crust-mantle transition and crustal geometry.

The electrical structure of the crust is highly heterogeneous towards the southwest in each model (Fig. 6). In contrast, broad, highly resistive (>30,000 Ω-m) crustal blocks R3 and R8 are revealed beneath stations 108–110 and 205–207, extending up to a depth of about 30 km, respectively. Towards the southwest, the crust is slightly less resistive in the TGM model than in the HYY model, and both models contain resistive and conductive features. A ~20 km thick conductor C2 (~20–70 Ω-m) is identified in the upper crust beneath station 103, which lies between resistive features R1 (~3000 Ω-m) and R2 (~25,000 Ω-m). A ~20 km thick conductor C3 (~100 Ω-m) is identified in the lower crust beneath stations 106–107, surrounded by a low-resistivity (~200 Ω-m) zone extending to the upper mantle. Towards the southwest, beneath station 101, a regional conductive feature, C1, is rising to a depth of ~20 km. The HYY model contains a crustal conductor and two moderate resistivity features separated by highly resistive components. A ~8 km thick, highly conductive C5 (~1–20 Ω-m) feature within a low-resistivity (~200 Ω-m) zone is identified beneath stations 203–204. Conductor C5 appears in resistive feature R7, and its maximum resistivity (~30,000 Ω-m) is marked beneath station 204 and indicates its attrition on all sides of C5 with depth beneath stations 203–204. A highly resistive (>30,000 Ω-m) and

~8 km thick feature R6 is associated with a steep moderate resistive (~500 Ω-m) zone towards the southwest of station 201. R6 overlies a nearly vertical moderate resistive (~800 Ω-m) feature C4, extending to a depth of about 40 km with increasing resistivity. These intermediate resistivity zones are equivalent to the resistivity of Proterozoic sediments identified in the basin structure. While the crustal network beneath stations 101–108 is low resistive, indicating conductive factors highly alter the crust compared to the HYY model.

The crust-mantle transition is a weak zone well defined by velocity contrast and known as 'seismic Moho' (Prodehl et al., 2013). The MT method helps identify the crust-mantle transition, i.e., 'electrical Moho' (Jones, 2013), although only in a few structural settings with low resistive zone or resistivity interface. The conductive lower crust limits the ability of the MT method to resolve interface over standard resistive upper-mantle structure (Jones, 1999) or in the case of highly resistive lithosphere structure. The Moho depth is a more helpful parameter for understanding deep tectonics of the upper lithospheric mantle, which altered the crustal structure. The crust-mantle transition in the Archean Slave craton is identified at ~36 km depth with upper-mantle resistivity ~4000 Ω-m (Jones and Ferguson, 2001) and ~46 km depth with upper-mantle resistivity ~730 Ω-m in the Archean Singhbhum craton (Bhattacharya and Shalivahan, 2002). In both cases, the crust is highly resistive and contains layers, and the data from the Slave craton also compare well with the seismic result (Jones and Ferguson, 2001). However, there is no evidence of deep upper-mantle structure in the Singhbhum craton. They interpreted electrical Moho or resistivity interface as a region with conductance less than 1 Siemens in the crustal structure (Jones and Ferguson, 2001).

In our study, the sharp resistivity contrast is marked at ~28 km depth beneath resistivity (>30,000 Ω-m) features R3 and R9. These features have conductance less than 1 Siemens where the upper-mantle zone is ~10 km thick with resistivity ~2000 Ω-m. HYY model shows moderate resistive (~3000 Ω-m) in a depth range of 35–45 km towards the southwest, where the crustal structure is highly heterogeneous. A resistive interface is marked beneath stations 102–105 in a depth range of 35–45 km towards the southwest, where the crustal structure is low resistive. The crust-mantle transition is not sharp towards the southwest, which may have been altered by deep tectonics in both modes. These weak zones are comparable with other geophysical responses of Moho in the study region and lie in the depth range of 30–45 km (Borah et al., 2014; Kumar et al., 2014). Thus, the electrical models from the present study suggest an almost identical depth range of crust-mantle transition or weak zone, which may be the root of electrical Moho in the study regions.

Many complex E-W, NE-SW, and NW-SE patterns, trending faults of varying dimensions, crosscut the basin (Fig. 1b). Sridhar et al. (2018) identified magnetic lineaments in the basin and interpreted (NE-SW/E-W/N-S trends) intra-basinal and deep (NW-SE trends) faults. Therefore, resistivity/conductivity interfaces in each electrical structure are compared with the above finding to outline the geometry of the crustal faults along both profiles (Fig. 8). The NW-SE trending lineaments (L1 to L7) are almost perpendicular to both profiles; NE-SW trending lineament L8 crosses both profiles, while E-W trending lineament L9 crosses only the TGM profile. The C4 feature is associated with L1 and L2 lineaments. The C2 feature is associated with L1 and L6 lineaments. The fault (F3) boundary identified towards the southwest of C4 and C2 extends up to a depth of ~15 km, while the fault (F4) boundary identified towards the northeast of these features extends to a depth of ~25 km. L2 and L6 lineaments may be a single unit, but resistivity contrast in these features and difference in fault slant suggest different tectonics associated with these fea-
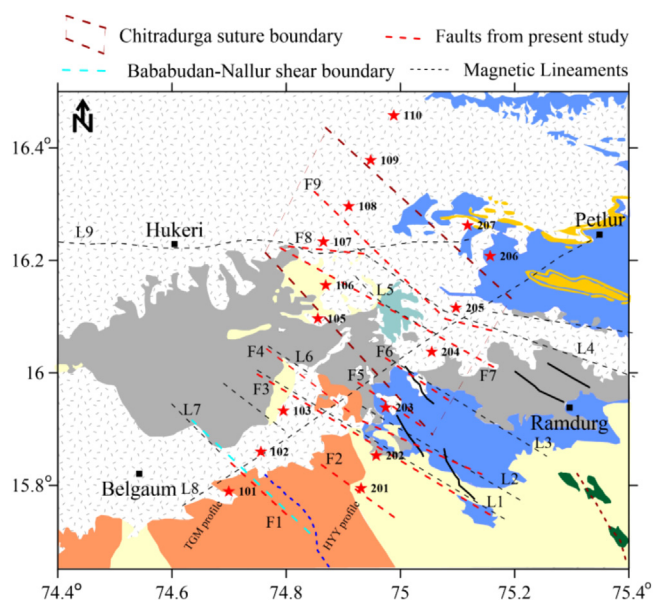

Fig. 8. Geological map with crustal faults and Archean suture boundaries at upper-mantle depth interpreted from present studies; most of the trend of the fault is associated with magnetic lineaments (Sridhar et al., 2018).

tures. C5 feature is associated with L3 lineament and a deep fault near station 203; these faults (F5 and F6) are steep and extend to a depth of ~20 km. Fault (F2) adjacent to station 201 extends to a depth of ~8 km; it may be an NW-SE trending steep fault. Fault (F1) adjacent to station 102 is southwest dipping, extending up to a depth of ~12 km, or beyond that, its NW-SE trend may continue up to L7 lineament towards the west. The southwest dipping fault (F7), marked near stations 106 and 204, is associated with the L5 lineament, and the northeast dipping fault (F9), kept near stations 108 and 205, is related to the L4 lineament. The difference in fault slant and low resistive zone beneath these stations suggest that crustal structure altered through different deep tectonics around these regions. Thus, F7 and F9 may be deep faults, and their NW-SE trends may continue up to Ramdurg regions towards the east. The northeast dipping fault (F8) near station 107 extends to a depth of ~10 km and may be an E-W trending fault associated with the L9 lineament.

5.3. Lithospheric upper-mantle structure

The lithosphere upper-mantle electrical structure contains a steep conductive feature C6 (~20 Ω-m) in the HYY model (Fig. 6). Feature C6 extends up to a depth of ~55 km with a conductivity of ~100 Ω-m beneath stations 204–205. The triangular shape low resistive zone beneath stations 204–205 may be a zone of Archean suture along which two domains of Dharwar craton were assembled at around 2.56–2.50 Ga. Thus, a ~25 km wider conductive area lies between upper-mantle resistive features (R9 and R10) and is interpreted as an Archean upper-mantle suture or Chitradurga Suture Zone (CSZ). Other geophysical methods also identify the Chitradurga boundary thrust (Ramadass et al., 2004) and Chitradurga shear boundary-associated lineaments (Rajaram and Anand, 2014; Rajaram et al., 2016). Across the north-south trend of Chitradurga shear, a broad conductive feature is revealed in the upper mantle (Gokarn et al., 2004), while Malleswari et al. (2019) identified the eastern boundary of Chitradurga shear beneath ~90 km depth and other associated conductive features beneath ~100 km depth altogether interpreted suture beneath western and eastern Dharwar craton. Beneath the Dharwar craton, uppermost mantle conductors are identified at the

depth range of 80–200 km (Kusham et al., 2021a, 2021b), where lithospheric thickness is reported to be more than 200 km. The Chitradurga Suture Zone is well identified in the HYY model, which extends up to the upper mantle lithosphere, and its signatures are apparent in the crustal section. The CSZ is a low resistive steep feature in the TGM model (Fig. 6), with ~25 km wide resistivity (~500 Ω-m) and lies between upper-mantle resistive features R4 and R5, rising to depth ~55 km. The CSZ identified in the TGM model underlies lower crustal conductor C3 (~100–200 Ω-m). The CSZ identified in both electrical models shows significant resistivity contrast. Another regional conductive feature (C1) is revealed beneath stations 101–102 in the TGM model with conductivity (~100–250 Ω-m). C1 rises to a depth of ~15 km and is interpreted eastern boundary of the Bababudan-Nallur Shear (BNS). The BNS may not appear in the HYY model due to limited profile coverage towards the southwest. This boundary is interpreted as the Bababudan-Nallur Shear by (Ramadass et al., 2004), which is now interpreted as the eastern boundary of the BNS and marked by an F1 fault in the upper crust and may be associated with L7 lineament. Thus, MT profile coverage towards the southwest may provide the western boundary of the BNS. The CSZ boundaries along its NNW trend revealed in both models and the BNS boundary in the TGM model at upper-mantle depth are shown on the geological map (Fig. 8).

5.4. Cause of enhanced conductivity at crustal and upper mantle depths

Many factors cause enhanced conductivity in the continental crust and lithospheric mantle: aqueous fluids, partial melting, sulfide, graphite, oxides of the ore body, and water (Nover, 2005; Yoshino, 2010; Pommier, 2013; Selway, 2014). These factors are governed by the interconnection of fluids, temperature, oxygen fugacity, pressure conditions, and geological history (Shankland, 1975; Lastovickova, 1991; Xu et al., 2000b; Jones et al., 2009).

The presence of aqueous fluids in the crust depends on the temperature and chloride content (Nesbitt, 1993). Still, fluids fail to increase their conductivity if the mobility of fluids is arrested in certain situations, like the closure of depth cracks (ELEKTB Group, 1997). The stress regime is essential in fluid interconnectivity in the continental crust (Gough, 1986). In a ductile regime with porosities, less than 0.5% of fluids enhance, leading to a conductivity increase (Wannamaker et al., 2008). However, fluids can be retained on a time scale during plate reformation (Goldfarb et al., 1991). The lower crust can be wet if sufficient liquid is available (Hyndman et al., 1993), which may be sourced from the subduction of wet rocks, fluid exsolution from cooling magma, or melting in the deep crust or upper mantle (Nur and Walder, 1990; Rice, 1992). The melting of rocks is highly temperature-dependent and slightly depends on pressure, water, and oxygen fugacity (Xu et al., 2000a, 2000b). Thus, the presence of melt may explain high conductivity at specific locations. The ion mobility increases with increasing temperature, decreasing pressure, and adding water to melt (Waff and Weill, 1975; Roberts and Tyburczy, 1999). The Dharwar craton, however, is characterized by a cold regime due to low heat flow with a mean value of 40 mW/m^2 (Roy and Rao, 2000), so partial melting in the crust can be excluded as the cause of conductivity increase. In stable tectonic regimes, high conductivity is explained by corresponding sulfide (Livelybrooks et al., 1996; Jones et al., 1997; Gokarn et al., 2004; Jones et al., 2005). However, sulfide minerals such as pyrite are reported in minor amounts in the basin (Jayaprakash, 2007).

Graphite occurs in carbon sheets with intercalated material, and interconnected graphite (grain-boundary graphite films on minerals) enhances electric conductivity (Frost et al., 1989;

Jodicke, 1985). Although stable at 600–900°C (Mathez, 1987; Mathez et al., 1984; Pineau and Mathez, 1990), they may not be stable at shallow depth due to low pressure (Katsube and Mareschal, 1993; Duba et al., 1988). Haak et al. (1991) explained low resistivity in the crust by graphite with low oxygen fugacity. At more oxidizing conditions, graphite becomes unstable, converting to carbonate minerals below the solidus and a carbon-rich melt above the solidus (Selway, 2014). The hydrogen (water) content in nominally anhydrous minerals enhances electrical conductivity (Karato, 1990, 2011; Huang et al., 2005), although it behaves as an incompatible element that is removed during melting or high temperature (Karato, 2019). Pressure reduces hydrogen-assisted electric conductivity (Dai and Karato, 2014a). Both of these are controlled by tectonic events in the lithosphere mantle (Selway, 2014). The lithosphere can be enriched in incompatible elements through interaction with fluids from a subducting slab (Reynard et al., 2011; Wang et al., 2012). The hydrogen contents (in olivine) originating from dehydration of subducting slabs increases conductivity (Brasse and Eydam, 2008), although conductivity increase with water contents and decrease with oxygen fugacity (Karato and Dai, 2009; Dai and Karato, 2014b). The less iron in the lithospheric mantle and carbon in the form of fluids inclusion fail to increase conductivity (Selway, 2014). CO_2-rich fluids derived from the deep mantle may enhance conductivity in less deformed lithospheric regions (ten Grotenhuis et al., 2004). The carbon sources in the mantle are separated by $\delta^{13}C$ isotope value (Pearson et al., 1994); heavy ~−5% and light ~−25% isotopes represent mantle sources and subducted organic matter sources, respectively. In the Kaladgi rift basin, high concentrations of methane (250 ppb) and light $\delta^{13}C$ (−29.9 to −39%) signatures may represent the thermogenic sources of carbon (Kalpana et al., 2010). The low contents of graphite fail to enhance conductivity (Santos et al., 2002), and no evidence is available for volcanic xenoliths in the study regions.

Mantle plumes originate from the mantle transition zone or the core-mantle boundary (Hofmann, 1997; Zhao, 2001), and plume-indicated magmatism is characterized by enrichment in incompatible elements (Dixon et al., 2002; Workman et al., 2006). However, the interaction of plumes with the lithosphere leads to partial melting and refertilization of the crust-mantle structure (Selway, 2014). Refertilization of the mantle by fluids is expected to lead to long-lived enhanced conductivity (Demouchy, 2010). The upper-mantle high conductivity is explained by partial molten rock sources from subducting slab and collision orogeny (Glover et al., 2000; Ledo et al., 2000), and associated fine-grain boundaries enhanced conductivity in lower crust (ten Grotenhuis et al., 2004). The coarse-grained (olivine) boundaries reduce the conductivity. The alkalic, silicate, and carbonate melts enhanced conductivity, and volatile riche alkalic melt with a small melt fraction may explain conductivity in the upper mantle (Hirschmann, 2010). However, silicate melt depends on the interconnectivity and requires a vast melt fraction (Tyburczy and Waff, 1983). The carbonate melts are more conductive than alkalic and silicate melts (Gaillard et al., 2008), and tiny malt fractions produce bulk conductivity due to their highly interconnected melts (Yoshino et al., 2010, 2012). Basalt melts in the upper mantle increase conductivity (Roberts and Tyburczy, 1999). Sulfide combined with basaltic melts (Ducea and Park, 2000) or the interconnected network (Watson et al., 2010) enhanced bulk conductivity.

The electrical models (Fig. 6) show significant conductivity variations along both profiles. This may suggest the influence of deep tectonics associated with study regions. The Archean collision between two subcontinents of the Dharwar craton is the source of upper-mantle suture and crustal fault/shear. Deccan basalts cover the Peninsular Indian Shield; therefore, crust and upper-mantle regimes were modified during the journey of the Indian Plate over the Reunion hotspot (Raval, 1999). The present structures produced
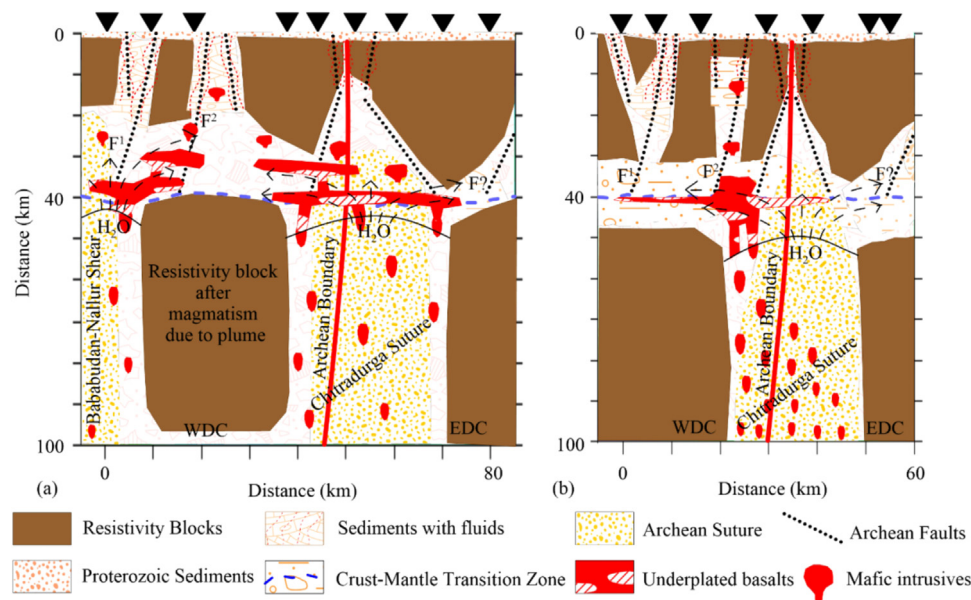
Fig. 9. The geological interpretation of electrical models through cartoon sketch, (a) along the TGM profile and (b) along the HYY profile. WDC – western Dharwar craton and EDC – eastern Dharwar craton.

from MT data indicate a significant effect of deep tectonics, which modified the lithospheric structures during the late-Archean to Tertiary period. Over geological periods structural conductivity may be controlled by several factors, as discussed above. The upper mantle shear zones can be explained by partially molten rocks formed by collision, and enhanced conductivity may be under grain size control. Fine-grained boundaries may be one possibility for the conductive lower crust in the TGM model; even though CSZ indicates decreased conductivity, possibly suggesting a conductive lower crust source from BNS, the entire region was modified by Reunion plume between the Cretaceous-Tertiary periods. During the Proterozoic, several small ocean basins were opened due to rifting and thermal subsidence along the suture. In this process, seawater incursion is the basin sediment source. The carbonate-rich fluids may be trapped in the crust through faults/fractures weakening the upper crust or enhancing conductivity, which may be altered later over geological time.

The large plume head weakens the lithosphere due to the influx of heat and melts/fluids (White and McKenzie, 1989). The hot material from the plume source continues to flow up, melting the mantle to produce voluminous basalts (Campbell and Griffiths, 1990) enriched in incompatible elements. Basaltic melt may be the leading cause of enhanced conductivity in the crust and upper-mantle structure. Several basaltic flows are identified in the basin regions near Gokak and Bagalkot (Jayaprakash, 2007). The magmatic underplating during the plume-induced crust-mantle interaction resulted in high density/high-velocity layer and low-resistive body (Tewari et al., 1991; Mall et al., 1999; Naganjaneyulu and Santosh, 2010b) in the lower crust. Low resistivity may be due to melts/fluids rising to the surface through faults/fractures. The regional Bouguer gravity anomaly indicates peaks and rapidly decreasing contour lines, as shown in Supplementary Data, Fig. S7, associated with crustal conductive features. Rapidly decreasing gravity value is attributed to a faulted and over-thrust boundary at gravity-low or high-density bodies (Naganjaneyulu and Santosh, 2010a). The moderate resistive feature C4 is associated with rapidly decreasing gravity between stations 202–203. The contour peaks from gravity low −110 to −95 mGal are related to upper crustal conductor C5 between stations 203–204. The region between stations 203–206 indicates a low gravity value compared to stations 105–108. The high and

low gravity indicates the crustal block's uplift and subsidence (Mishra et al., 2000). Thus, the conductive lower crust beneath stations 101–108 may demonstrate uniform gravity value, and the gravity value beneath stations 201–205 may explain the heterogeneity of the crust. The crust in the northeast section of the profiles is resistive, homogenous, and denser, and the resistivity contrast of R3 and R8 may explain the change in gravity value in the region. Electrical structures produced from present studies support regional gravity finding by Kailasam et al. (1972).

5.5. Interpretation from electrical models

The Kaladgi rift basin was subject to different pulses of deformation, uplift, new basin formation, polyphase magmatism, and regional metamorphism. The crustal features C2 and C4 have similar structures associated with faults F3 and F4, and the surrounding area is marked by sizeable intrusive dyke swarms. Significant resistivity contrast in between and change in faults indicate different tectonic activity around these regions. C4 overlies upper-mantle resistive feature R9. The crustal features around stations 201–202 are equivalent to the resistivities of Proterozoic sediments. These moderate resistivity features are interpreted as carbonate trapped in faults/fractures during the basin formation. The lower crustal region was altered by fluids released from the deep mantle during plume activity. Conductor C5 is revealed in steep resistive zones associated with CSZ and is interpreted as mafic intrusions derived from underplated basalts in the sulfide fluids mixed material. The conductive features C2 and C3 indicate their attrition, C2 overlies upper-mantle resistive feature R4, and C1 and C3 overlap suture zones. The low resistive feature R4 lies between Archean sutures and may indicate reformation through magmatism and the generation of dyke swarms. The mantle material induced by the plume causes features C1, C2, and C3, interpreted as mafic intrusions derived from underplated basalts and fluids.

As discussed above, the crustal geometry beneath the western section of the Kaladgi rift basin and adjacent regions indicate that the NW-SE trending crustal faults mainly control the basin structure (Fig. 8). The geological history of the study region from the Late Archean to the Late Cretaceous periods is explained through a cartoon sketch along both profiles (Fig. 9). Two domains of the Dharwar craton were assembled along the Archean bound-

ary. The collision produced the suture zone (CSZ) at ~2.56–2.50 Ga. The associated crustal faults/fractures (F[1], F[2] and F?) in the related domains resulted in the rift zone. Magmatism during Paleoproterozoic (~1.9–1.6 Ga) through plume activity is recorded by the deposition of older sediments in the basin (Mishra, 2011), as also reported from other rift-related basins (French et al., 2008; Rogers and Santosh, 2009). Younger sediments of the basin were sourced from surface erosion (Jayaprakash, 2007). Many dyke swarms are exposed in the basin and are the same age (Jayaprakash, 2007) or older (French et al., 2008). Late Archean collision resulted in a ~25 km wider suture (CSZ), and the crustal faults, magmatism, and fluid flux weakened the crust and upper-mantle structure. Several factors discussed above cause enhanced crust and upper-mantle structure conductivities. Fault F[1] and Archean boundary beneath the TGM profile are part of BNS and CSZ, and these sutures may have altered the entire structure beneath the TGM profile compared to the HYY profile. At the same time, the structure beneath the HYY profile is dominated by CSZ. During the Cretaceous-Tertiary periods, the large plume head weakened the lithosphere. Faults F[2] beneath the TGM profile and F[1] beneath the HYY profile are considered in a line where F[2] is altered by basaltic melts and fluids derived from underplated mangle magmas. Basaltic melts alter fault F[1]. Wider and narrow weak zones associated with CSZ in the lower crust suggest magmatism relatively large beneath the TGM profile. The basaltic melts and fluids altered the lower crust beneath the TGM profile. Basaltic melts remained in CSZ, with only fluids changing the lower crust and crust-mantle transition zone beneath the HYY profile. Fault F[1] beneath the HYY profile was altered through liquids and carbonate/sulfide fluids. Thus, over geological time, the conductivity was enhanced by fluids from the surface that penetrated deep through fault/fracture, mafic intrusions derived from underplated basalts, and fluids from depth related to a mantle plume.

6. Summary and conclusions

The electrical structures in the western section of the Kaladgi rift basin provide evidence of deep tectonics during the late Archean to Tertiary periods. The MT method imaged a complex structure beneath the basin through conductivity variation. A ~100 m thick Deccan basalt is revealed along the TGM profile and overlies a flat layer of Badami Group sediments. The undulating layers beneath the HYY profile show apparent deformation of the Bagalkot Group sediments. Proterozoic deposits are in the depth range of ~500–1500 m with resistivity ~100–700 Ω-m, and fault/fracture zones may contain older sediment s indicating moderate resistivity. The high conductive patches are attributed to the rock composition; since station spacing is large, more data will better constrain the top layers up to 1000 m. The crustal structure mainly comprises NW-SE trending faults and a resistive interface apparent in their orientation. The crustal geometry helps to evaluate the deep tectonics that altered the entire structure and produced conductive features. The structure beneath the study area was shaped by collisional suturing, plume tectonics and rifting, and intense magmatism and fluid activity. The upper crust is mostly fractured along both profiles, and these fractures may be filled by carbonate fluids that penetrate depth through weak zones beneath the Proterozoic basin. The Archean sutures altered the upper-mantle resistive feature in the TGM model, and magmatism during rifting enhanced the conductivity in the upper mantle. The entire lithospheric structure was modified during the Cretaceous-Tertiary periods over the Reunion plume. The basaltic melts and fluids from the deep mantle from plume activity enhanced the conductivity in the lower crust and crust-mantle transition zone. The crust-mantle transition zone is marked between depth ranges ~30–45 km along both profiles and suggests the area

of electrical Moho. The NNW trend of CSZ at the upper mantle is ~25 km wider, and its conductivity might have been altered during the Cretaceous-Tertiary period beneath these profiles. The BNS may be a more extensive zone extending towards the southwest. Our MT study provides insights into the lithologic and structural architecture of the Paleoproterozoic intracratonic rift basin. Our findings might be helpful for regional geodynamic reconstructions and deep exploration activities.

Declaration of Competing Interest

The authors declare that they have no known competing financial interests or personal relationships that could have appeared to influence the work reported in this paper.

CRediT authorship contribution statement

Amit Kumar: Formal analysis, Investigation, Methodology, Software, Writing – original draft. **Danda Nagarjuna:** Visualization, Writing – review & editing. **M. Santosh:** Conceptualization, Writing – review & editing, Supervision, Validation. **S.K. Begum:** Data curation. **C.K. Rao:** Data curation, Conceptualization, Supervision.

Acknowledgments

Supplementary materials

Supplementary material associated with this article can be found, in the online version, at doi:10.1016/j.geogeo.2023.100236.

References

Abdul Azeez, K.K., Veeraswamy, K., Gupta, A.K., Babu, N., Chandrapuri, S., Harinarayana, T., 2015. The electrical resistivity structure of lithosphere across the Dharwar craton nucleus and Coorg block of South Indian shield: evidence of collision and modified and preserved lithosphere. J. Geophys. Res. Solid Earth 120. doi:10.1002/2014JB011854.

Anand, S.P., Erram, V.C., Patil, J.D., Pawar, N.J., Gupta, G., Suryavanshi, R.A., 2016. Structural mapping of Chikotra River Basin in the Deccan Volcanic Province of Maharashtra, India from ground magnetic data. J. Earth Syst. Sci. 125 (2), 301–310.

Anand, S.P., Rajaram, M., 2002. Aeromagnetic data to probe the Dharwar Craton. Curr. Sci. 83 (2), 34–52.

Bahr, K., 1988. Interpretation of the magnetotelluric impedance tensor: regional induction and local telluric distortion. J. Geophys. 62, 119–127.

Balakrishnan, S., Rajamani, V., Hanson, G.N., 1999. U-Pb ages for Zircon and Titanite from the Ramagiri area, Southern India: evidence for accretionary origin of the Eastern Dharwar craton during the Late Archean. J. Geology 107, 69–86.

Bhattacharya, B.B., Shalivahan, 2002. The electric Moho underneath Eastern Indian Craton. Geophys. Res. Lett. 29, 1376. doi:10.1029/2001GL014062.

Borah, K., Rai, S., Gupta, S., Prakasam, K., Kumar, S., Sivaram, K., 2014. Preserved and modified mid-Archean crustal blocks in Dharwar Craton: seismological evidence. Precambrian Res 246, 16–34. doi:10.1016/j.precamres.2014.02.003.

Brasse, H., Eydam, D., 2008. Electrical conductivity beneath the Bolivian Orocline and its relation to subduction processes at the South American continental margin. J. Geophys. Res. 113, B07109. doi:10.1029/2007JB005142.

Brasse, H., Lezaeta, P., Rath, V., Schwalenberg, K., Soyer, W., Haak, V., 2002. The Bolivian altiplano conductivity anomaly. J. Geophys. Res. 107 (B5). doi:10.1029/2001JB000391.0.

Caldwell, T.G., Bibby, H.M., Brown, C., 2004. The magnetotelluric phase tensor. Geophys. J. Int. 158, 457–469.

Campbell, I.H., Griffiths, R.W., 1990. Implications of mantle plume structure for the evolution of flood basalts. Earth Planet. Sci. Lett. 99, 79–93.

Chadwick, B., Ramakrishnan, M., Viswanatha, M.N., 1985. Bababudan a Late Archaean intracratonic volcanosedimentary basin, Karnataka, South India. Part I: stratigraphy and basin development. J. Geol. Soc. India 26, 769–801.

Chadwick, B., Ramakrishnan, M., Viswanatha, M.N., 1981. The stratigraphy and structure of the Chitradurga region an illustration of cover-basement interaction in the late Archean evolution of the Karnataka craton, southern India. Precambrian Res. 16, 31–54.

Chadwick, B., Vasudev, V.N., Hegde, G.V., 2000. The Dharwar craton, southern India, interpreted as the result of late Archaean oblique convergence. Precambrian Res. 99, 91–101.

Chardon, D., Jayananda, M., Chetty, T.R.K., Peucat, J.J., 2008. Precambrian continental strain and shear zone patterns: the South Indian case. J. Geophys. Res. 113, B08402. doi:10.1029/2007JB005299.

Chu, X., Zhang, T., Zhang, Q., Lyons, T.W., 2007. Sulfur and carbon isotope records from 1700 to 800 Ma carbonates of the Jixian section, northern China: implications for secular isotope variations in Proterozoic seawater and relationships to global supercontinental events. Geochim. Cosmochim. Acta. 71, 4668–4692.

Dai, L., Karato, S., 2014a. The effect of pressure on hydrogen-assisted electrical conductivity of olivine. Phys. Earth Planet. Inter. 232, 51–56.

Dai, L., Karato, S., 2014b. Influence of oxygen fugacity on the electrical conductivity of hydrous olivine Implications for the mechanism of conduction. Phys. Earth Planet. Inter. 232, 57–60.

Demouchy, S., 2010. Diffusion of hydrogen in olivine grain boundaries and implications for the survival of water-rich zones in the Earth's mantle. Earth Planet. Sci. Lett. 295, 305–313.

Danda, N., Rao, C.K., 2019. Magnetotelluric study to characterize sediment thickness across Kachchh and Cambay rift basins, western India. Curr. Sci. 116 (2), 299–304.

Danda, N., Rao, C.K., Kumar, A., 2017. Geoelectric structure of northern Cambay rift Basin from magnetotelluric data. Earth Planet. Space 69, 140. doi:10.1186/s40623-017-0725-0.

Danda, N., Rao, C.K., Kumar, A., Rao, P.R., Subba Rao, P.B.V., 2020. Implications for the lithospheric structure of Cambay rift zone, western India: inferences from a magnetotelluric study. Geosci. Front. 11, 1743–1754. doi:10.1016/j.gsf.2020.01.014.

Danda, N., Rao, C.K., Pavankumar, G., Kumar, A., Manglik, A., 2021. Magnetotelluric evidence for an Archaean-Proterozoic lithospheric assemblage within the Cambay rift basin, western India, and its role in channeling of plume-derived fluids within the basin. Tectonophysics 818, 229064. doi:10.1016/j.tecto.2021.229064.

Danda, N., Kumar, A., Pavankumar, G., Rao, C.K., Manglik, A., 2023. Spatially heterogeneous lithospheric architecture of the Cambay rift basin and adjoining Aravalli-Delhi fold belt, western India - a synthesis of magnetotelluric results. Tectonophysics 861, 229905.

Dixon, J.E., Leist, L., Langmuir, C., Schilling, J.G., 2002. Recycled dehydrated lithosphere observed in plume influenced mid-ocean-ridge basalt. Nature 420 (6914), 385–389.

Duba, A., Huenges, E., Nover, G., Will, G., Jodicke, H., 1988. Impedance of black shale from Munsterland-1 borehole-an anomalously good conductor. Geophys. J. Int. 94 (3), 413–419. doi:10.1111/j.1365-246X.1988.tb02264.x.

Ducea, M.N., Park, S.K., 2000. Enhanced mantle conductivity from sulfide minerals, southern Sierra Nevada, California. Geophys. Res. Lett. 27 (16), 2405–2408.

ELEKTB Group, 1997. KTB and the electrical conductivity of the crust. J. Geophys. Res. 102, 18289–18305.

French, J.E., Heamana, L.M., Chacko, T., Srivastava, R.K., 2008. 1891-1883 Ma Southern Bastar-Cuddapah mafic igneous events India a newly recognized large igneous province. Precambrian Res. 160, 308–322.

Frost, B.R., Fyfe, W.S., Tamki, K., Chart, T., 1989. Grain-boundary graphite in rocks and implications for high electrical conductivity in the lower crust. Nature 340, 134–136.

Gaillard, F., Marki, M., Iacono-Marziano, G., Pichavant, M., Scaillet, B., 2008. Carbonatite melts and electrical conductivity in the asthenosphere. Science 32, 1363–1365.

Gautam, S., 2001. Generation of Deccan trap magmas. Proc. Indian Acad. Sci. Earth Planet. Sci. 110, 409–431.

Gao, P., Santosh, M., 2020. Mesoarchean accretionary mélange and tectonic erosion in the Archean Dharwar Craton, southern India: plate tectonics in the early Earth. Gondwana Res 85, 291–305.

Glover, P.W.J., Pous, J., Queralt, P., Munoz, J.A., Liesa, M., Hole, M.J., 2000. Integrated two-dimensional lithospheric conductivity modelling in the pyrenees using field-scale and laboratory measurements. Earth Planet. Sci. Lett. 178, 59–72.

Gokarn, S.G., Gupta, G., Rao, C.K., 2004. Geoelectric structure of the Dharwar craton from magnetotelluric studies: Archean suture identified along the Chitradurga–Gadag schist belt. Geophys. J. Int. 158, 712–728.

Gokarn, S.G., Gupta, G., Rao, C.K., Selvaraj, C., 2003. Some interesting observations on the tectonics in the Deccan volanic province observed from magnetotelluric studies. J. Virtual Explor. 12, 55–65.

Gokarn, S.G., Rao, C.K., Singh, B.P., Nayak, P.N., 1992. Magnetotelluric studies across the Kurduwadi gravity feature. Phys. Earth Planet. Inter. 72, 58–67.

Goldfarb, R.J., Snee, L.W., Miller, L.D., Newberry, R.J., 1991. Rapid dewatering of the crust deduced from ages of mesothermal gold deposits. Nature 354, 296–298.

Gough, D.I., 1986. Seismic reflectors, conductivity, water and stress in the continental crust. Nature 323, 143–144.

Groom, R.W., Bailey, R.C., 1989. Decomposition of the magnetotelluric impedance tensor in the presence of local three-dimensional galvanic distortions. J. Geophys. Res. 94, 1913–1925.

Gupta, S., Rai, S.S., Prakasam, K.S., Srinagesh, D., Bansal, B.K., Chadha, R.K., Preistley, K., Gaur, V.K., 2003. The nature of the crust in southern India: implications for Precambrian crustal evolution. Geophys. Res. Lett. 30, 1419. doi:10.1029/2002GL016770.

Haak, V., Stoll, J., Winteral, H., 1991. Why is the electrical resistivity around the KTB hole so low? Phys. Earth Planet. Inter. 66, 12–23.

Hansen, P.C., 1998. Rank Deficient and Discrete Ill-posed problems, Numerical Aspects of Linear Inversion. SIAM, Philadelphia.

Hirschmann, M.M., 2010. Partial melt in the oceanic low velocity zone. Phys. Earth Planet. Inter. 179, 60–71.

Hofmann, A.W., 1997. Mantle geochemistry: the message from oceanic volcanism. Nature 385 (6613), 219–229. doi:10.1038/385219a0.

Hou, G., Santosh, M., Qian, X., Lister, G.S., Li, J., 2008. Configuration of the late Paleoproterozoic supercontinent Columbia insights from radiating mafic dyke. Precambrian Res. 14, 395–409.

Huang, X., Xu, Y., Karato, S., 2005. Water content of the mantle transition zone from the electrical conductivity of wadsleyite and ringwoodite. Nature 434, 746–749.

Hyndman, R.D., Vanyan, L.L., Marquis, G., Law, L.K., 1993. The origin of electrically conductive lower continental crust saline water or graphite. Phys. Earth Planet. Inter. 81, 325–344.

Jagadeesh, S., Rai, S.S., 2008. Thickness, composition, and evolution of the Indian Precambrian crust inferred from broadband seismological measurements. Precambrian Res. 162 (1–2), 4–15.

Jayananda, M., Aadhiseshan, K.R., Kusiak, M.A., Wilde, S.A., Sekhamo, K.U., Guitreau, M., Santosh, M., Gireesh, R.V., 2020. Multi-stage crustal growth and Neoarchean geodynamics in the Eastern Dharwar Craton, southern India. Gondwana Res. 78, 228–260.

Jayananda, M., Banerjee, M., Pant, N.C., Dasgupta, S., Kano, T., Mahesha, N., Mahableswar, B., 2011. 2.62 Ga high-temperature metamorphism in the central part of the eastern Dharwar craton: implications for late Archaean tectonothermal history. Geol. J. 46. doi:10.1002/gj.1308.

Jayananda, M., Chardon, D., Peucat, J.J., Capdevila, R., Martin, H., 2006. 2.61 Ga potassic granites and crustal reworking, western Dharwar craton (India): tectonic, geochronologic and geochemical constraints. Precambrian Res. 150, 1–26.

Jayananda, M., Moyen, J.R., Martin, H., Peucat, J.J., Auvray, V., Mahabaleswar, B., 2000. Late Archean (2550-2520 Ma) juvenile magmatism in the eastern Dharwar craton, southern India: constraints from geochronology, Nd-Sr isotopes and whole rock geochemistry. Precambrian Res. 99, 225–254.

Jayananda, M., Tsutsumi, Y., Miyazaki, T., Gireesh, R.V., Kapfo, K., Tushipokla, Hidaka, H., Kano, T., 2013. Geochronological constraints on Meso- and Neoarchean regional metamorphism and magmatism in the Dharwar craton, southern India. J. Asian Earth Sci. 78, 18–38.

Jayaprakash, A.V., 2007. Purana basins of Karnataka. Memoir. Geol. Surv. India 129, 1–137.

Jayaprakash, A.V., Sundaram, V., Hans, S.K., Mishra, R.N., 1987. Geology of the Kaladgi-Badami basin, Karnataka. Memoir. Geol. Soc. India 6, 201–226.

Jiracek, G., 1990. Near-surface and topographic distortions in electromagnetic induction. Surv. Geophys. 11, 163–203.

Jodicke, H., 1985. A large self-potential anomaly at the SE Flank of the Stavelot-Venn anticline originating from meta-anthracite bearing black shales at the Salm/Revin boundary. Neues. Johrb. Geol. Polaenntol. Abh. 171, 387–402.

Johnston, D.T., Poulton, S.W., Fralick, P.W., Wing, B.A., Canfield, D.E., Farquhar, J., 2006. Evolution of the oceanic sulfur cycle at the end of the Paleoproterozoic. In: Canfield, D.E., Lyons, T.W., Morse, J.W. (Eds.), A special issue dedicated to Robert A. Berner. Geochim. Cosmochim. Acta 70, 5723–5739.

Jones, A.G., 1983. On the equivalence of the "Niblett" and "Bostick" transformations in the magnetotelluric method. J. Geophys. 53, 72–73.

Jones, A.G., 1999. Imaging the continental upper mantle using electromagnetic methods. Lithos 48 (1–4), 57–80.

Jones, A.G., 2013. Imaging and observing the electrical Moho. Tectonophysics 609, 423–436. doi:10.1016/j.tecto.2013.02.025.

Jones, A.G., Chave, A.D., Alud, D., Bahr, K., Egbert, G., 1989. A comparison of techniques for magnetotelluric response function estimation. J. Geophys. Res. 94, 14201–14213.

Jones, A.G., Ferguson, I.J., 2001. The electric Moho. Nature 409 (6818), 331–333.

Jones, A.G., Jodicke, H., 1984. Magnetotelluric transfer function estimation improvement by coherent based technique. In: Proceedings of the 54th Annual International Meeting of Soc. Expl. Geophysics. Atlanta, GA Dec. 2-6.

Jones, A.G., Evans, R.L., Eaton, D.W., 2009. Velocity-conductivity relationships for mantle mineral assemblages in Archean cratonic lithosphere based on a review of laboratory data and Hashin-Shtrikman extremal bounds. Lithos 109, 131–143.

Jones, A.G., Groom, R.G., 1993. Strike-angle determination from the magnetotelluric impedance tensor in the presence of noise and local distortion: rotate at your peril!. Geophys. J. Int. 113, 524–534. doi:10.1111/j.1365-246X.1993.tb00905.x.

Jones, A.G., Katsube, T.J., Schwann, P., 1997. The longest conductivity anomaly in the World explained: sulphides in fold hinges causing very high electrical anisotropy. J. Geomag. Geoelectr 49, 1619–1629.

Jones, A.G., Ledo, J., Ferguson, I.J., 2005. Electromagnetic images of the Trans-Hudson orogen the North American Central Plains anomaly revealed. Can. J. Earth Sci. 42, 457–478.

Joy, S., Patranabis-Deb, S., Saha, D., Jelsma, H., Maas, R., Soderlund, U., Tappe, S., Linde, G., Banerjee, A., Krishnan, U., 2018. Depositional history and provenance

of cratonic "Purana" basins in southern India: a multipronged geochronology approach to the Proterozoic Kaladgi and Bhima basins. Geolog. J. 1–28. doi:10.1002/gj.3415.

Kailasam, L.N., Murty, B.G.K., Chayanulu, A.Y.S.F., 1972. Regional gravity studies of the Deccan trap areas of the peninsular India. Geol. Surv. India 41, 403–407.

Kailasam, L.N., Reddy, A.G.B., Joga Rao, M.V., Sathyamurthy, K., Murty, B.S.R., 1976. Deep electrical resistivity sounding in the Deccan trap region. Curr. Sci. 45, 9–18.

Kale, V.S., Phansalkar, V.G., 1991. Purana basins of Peninsular India: a review. Basin Res. 3, 1–36.

Kalpana, M.S., Patil, D.J., Dayal, A.M., Raju, S.V., 2010. Near surface manifestation of hydrocarbons in proterozoic Bhima and Kaladgi basins: implications to hydrocarbon resource potential. Geol. Soc. India 76, 548–556.

Karato, S., 1990. The role of hydrogen in the electrical-conductivity of the upper mantle. Nature 347 (6290), 272–273. doi:10.1038/347272a0.

Karato, S., 2011. Water distribution across the mantle transition zone and its implications for global material circulation. Earth Planet. Sci. Lett. 301, 413–423.

Karato, S., 2019. Some remarks on hydrogen-assisted electrical conductivity in olivine and other minerals. Earth Planet. Sci. 6, 55. doi:10.1186/s40645-019-0301-2.

Karato, S., Dai, L., 2009. Comments on "Electrical conductivity of wadsleyite as a function of temperature and water content" by Manthilake et al. Phys. Earth Planet. Inter. 174, 19–21.

Krogstad, E.J., Hanson, G.N., Rajamani, V., 1991. U-Pb ages of zircon and sphene for two gneiss terranes adjacent to the Kolar Schist Belt, South India: evidence for separate crustal evolution histories. J. Geol. 99, 801–816.

Kumar, N., Zeyen, H., Singh, A.P., 2014. 3D lithosphere density structure of southern Indian Shield from joint inversion of gravity, geoid and topography data. J. Asian Earth Sci. 89, 98–107. doi:10.1016/j.jseaes.2014.03.028.

Kumar, A., Bhaskar Rao, Y.J., Sivaraman, T.V., Gopalan, K., 1996. Sm-Nd ages of Archaean metavolcanics of the Dharwar craton, South India. Precambrian Res. 80, 205–216.

Kusham, Naick, B.P., Pratap, A., Naganjaneyulu, K., 2021a. Magnetotelluric 3-D full tensor inversion in the Dharwar craton, India: mapping of subduction polarity and kimberlitic melt. Phys. Earth Planet. Inter. 315, 106708.

Kusham, Naick, B.P., Pratap, A., Naganjaneyulu, K., 2021b. 2-D versus 3-D Magnetotelluric Data Interpretation: a case study from the Dharwar craton. Tectonophysics 816, 229028.

Katsube, T.J., Mareschal, M., 1993. Petrophysical model of deep electrical conductors: graphite lining as a source and its disconnection due to uplift. J. Geophys. Res. 98 (B5), 8019–8030.

Lastovickova, M., 1991. A review of laboratory measurements of the electrical conductivity of rocks and minerals. Phys. Earth Planet. Inter. 66, 1–11.

Ledo, J., Ayala, C., Pous, J., Queralt, P., Marcuello, A., Munoz, J.A., 2000. New geophysical constraints on the deep structure of the Pyrenees. Geophys. Res. Lett. 27 (7), 1037–1040.

Ledo, J., Jones, A.G., Ferguson, I.J., Wolynec, L., 2004. Lithospheric structure of the Yukon, northern Canadian Cordillera, obtained from magnetotelluric data. J. Geophys. Res. 109, B04410. doi:10.1029/2003jb002516.

Ledo, J., Queralt, P., Marti, A., Jones, A.G., 2002. Two-dimensional interpretation of three-dimensional magnetotelluric data: an example of limitations and resolution. Geophys. J. Int. 150, 127–139.

Ledo, J., Queralt, P., Pous, J., 1998. Effects of galvanic distortion on magnetotelluric data over a three-dimensional regional structure. Geophys. J. Int. 132, 295–301.

Liang, H., Jin, S., Wei, W., Gao, R., Ye, G., Zhang, L., Yin, Y., Lu, Z., 2018. Lithospheric electrical structure of the middle Lhasa terrane in the south Tibetan plateau. Tectonophysics 731-732, 95–103.

Livelybrooks, D., Mareschal, M., Blais, E., Smith, J.T., 1996. Magnetotelluric delineation of the Trillabelle massive sulfide body in Sudbury, Ontario. Geophysics 61 (4), 971–986.

Mall, D.M., Rao, V.K., Reddy, P.R., 1999. Deep subcrustal features in the Bengal Basin: seismic signatures of plume activity. Geophys. Res. Lett. 26, 2545–2548.

Malleswari, D., Veeraswamy, K., Abdul Azeez, K.K., Gupta, A.K., Babu, N., Patro, P.K., Harinarayana, T., 2019. Magnetotelluric investigation of lithospheric electrical structure beneath the Dharwar Craton in south India: evidence for mantle suture and plume-continental interaction. Geosci. Front. 10 (5), 1915–1930. doi:10.1016/j.gsf.2018.10.011.

Mathez, E.A., 1987. Carbonaceous matter in mantle xenoliths composition and relevance to the isotopes. Geochim. Cosmochim. Acta 51 (9), 2339–2347. doi:10.1016/0016-7037(87)90288-2.

Mathez, E.A., Dietrich, V.J., Irving, A.J., 1984. The geochemistry of carbon in mantle peridotites. Geochim. Cosmochim. Acta 48 (9), 1849–1859. doi:10.1016/0016-7037(84)90038-3.

McNiece, G., Jones, A.G., 2001. Multistation, multifrequency tensor decomposition of magnetotelluric data. Geophysics 66, 158–173.

Meen, J.K., Rogers, J.J., Fullagar, P.D., 1992. Lead isotopic composition of the western Dharwar craton, southern India: evidence for distinct middle Archaean terrenes in a late Archaean craton. Geochim. Cosmochim. Acta 56, 2455–2470.

Meert, J.G., Santosh, M., 2017. The Columbia supercontinent revisited. Gondwana Res. 50, 67–83.

Mishra, D.C., 2011. Long hiatus in proterozoic sedimentation in India Vindhyan, Cuddapah and Pakhal Basins - a plate tectonic model. J. Geol. Soc. India 77, 17–25.

Mishra, D.C., Singh, B., Tiwari, V.M., Gupta, S.B., Rao, M.B.S.V., 2000. Two cases of continental collisions and related tectonics during the Proterozoic period in India-insights from gravity modelling constrained by seismic and magnetotelluric studies. Precambrian Res. 99, 149–169.

Mukherjee, M.K., Das, S., Modak, K., 2016. Basement-Cover structural relationships in the Kaladgi Basin, southwestern India: indications towards a Mesoproterozoic gravity gliding of the cover along a detached unconformity. Precambrian Res. 281, 495–520. doi:10.1016/j.precamres.2016.06.013-0310-9268.

Naganjaneyulu, K., Naidu, G.D., Rao, M.S., Shankar, K.R., Kishore, S.R.K., Murthy, D.N., Veeraswamy, K., Harinarayana, T., 2010. Deep crustal electromagnetic structure of central India tectonic zone and its implications. Phys. Earth Planet. Inter. 181, 60–68. doi:10.1016/j.pepi.2010.03.011.

Naganjaneyulu, K., Santosh, M., 2010a. The Cambrian collisional suture of Gondwana in southern India: a geophysical appraisal. J. Geodynam. 50, 256–267.

Naganjaneyulu, K., Santosh, M., 2010b. The central Indian tectonic zone: a geophysical perspective on continental amalgamation along a Mesoproterozoic suture. Gondwana Res. 18, 547–564. doi:10.1016/j.gr.2010.2.017.

Naganjaneyulu, K., Santosh, M., 2012. The nature and thickness of lithosphere beneath the Archean Dharwar craton, southern India: a magnetotelluric model. J. Asian Earth Sci. 49, 349–361.

Nance, R.D., Murphy, J.B., Santosh, M., 2014. The supercontinent cycle: a retrospective essay. Gondwana Res. 25, 4–29.

Naqvi, S.M., Khan, R.M.K., Manikyamba, C., Mohana, M.R., Khanna, T.C., 2006. Geochemistry of the NeoArchaean high-Mg basalts, boninites and adakites from the Kushtagi-Hungund greenstone belt of the Eastern Dharwar Craton (EDC); implications for the tectonic setting. J. Asian Earth Sci. 27, 25–44.

Nesbitt, B.E., 1993. Electrical resistivities of crustal fluids. J. Geophys. Res. 98, 4301–4310.

Nover, G., 2005. Electrical properties of crustal and mantle rocks- A review of laboratory measurements and their explanation. Surv. Geophys. 26, 593–651.

Nur, A., Walder, J., 1990. Time dependent hydraulics of the earth's crust. In: The Role of Fluids in Crustal Processes. National Academy Press, Washington, DC, pp. 113–127.

Nutman, A.P., Chadwick, B., Krishna Rao, B., Vasudev, V.N., 1996. SHRIMP U-Pb zircon ages of acid volcanic rocks in the Chitradurga and Sandur Groups and granites adjacent to Sandur schist belt. J. Geol. Soc. India 47, 153–161.

Ohmoto, H., Watanabe, Y., Kumazawa, K., 2004. Evidence from massive siderite beds for a CO_2-rich atmosphere before approximately 1.8 billion years ago. Nature 429, 395–399.

O'Neill, C., Muller, D., Steinberger, B., 2003. Geodynamic implications of moving Indian Ocean hotspots. Earth Planet. Sci. Lett. 215, 151–168. doi:10.1007/s40328-013-0039-z.

Padilha, A.L., Vitorello, I., de Pádua, M.B., Fuck, R.A., 2019. Magnetotelluric images of Paleoproterozoic accretion and Mesoproterozoic to Neoproterozoic reworking processes in the northern Sao Francisco Craton, central-eastern Brazil. Precambrian Res. 333, 105416.

Patro, P.K., Sarma, S.V.S., 2007. Trap thickness and the subtrappean structures related to mode of eruption in the Deccan plateau of India: results from magnetotellurics. Earth Planet. Space 59, 75–81. doi:10.1186/BF03352679.

Patro, P.K., Abdul Azeez, K.K., Veeraswamy, K., Sarma, S.V.S., Sen, M.K., 2015. Sub-basalt sediment imaging - the efficacy of magnetotellurics. J. App. Geophys. 121, 106–115.

Pearson, D., Boyd, F., Haggerty, S., Pasteris, J., Field, S., Nixon, P., Pokhilenko, N., 1994. The characterisation and origin of graphite in cratonic lithospheric mantle: a petrological carbon isotope and Raman spectroscopic study. Contrib. Miner. Petrol. 115 (4), 449–466.

Peucat, J.J., Mahabaleswar, B., Jayananda, M., 1993. Age of younger tonalitic magmatism and granulitic metamorphism in the South Indian transition zone (Krishnagiri area): comparison with older Peninsular gneisses from the Gorur-Hassan area. J. Metamorph. Geol. 11, 879–888.

Peucat, J.J., Jayananda, M., Chardon, D., Capdevila, R., Fanning, C.M., Paquette, L.J., 2013. The lower crust of the Dharwar Craton, Southern India patchwork of Archean granulitic domains. Precambrian Res. 227, 4–28.

Pineau, F., Mathez, E.A., 1990. Carbon isotopes in xenoliths from the Hualalai volcano, Hawaii, and the generation of isotopic variability. Geochim. Cosmoch. Acta 54 (1), 217–227. doi:10.1016/0016-7037(90)90209-4.

Pommier, A., 2013. Interpretation of magnetotelluric results using laboratory measurements. Surv. Geophys. doi:10.1007/s10712-013-9226-2.

Poulton, S.W., Fralick, P.W., Canfield, D.E., 2004. The transition to a sulphidic ocean approximately 1.84 billion years ago. Nature 431, 173–177.

Pratap, A., Kusham, Pradeep Naick, B., Naganjaneyulu, K., 2018. A magnetotelluric study from over Dharwar cratonic nucleus into Billigiri Rangan charnockitic massif, India. Phys. Earth Planet. Inter. 280, 32–39. doi:10.1016/j.pepi.2018.04.008.

Pratap, A., Pradeep Naick, B., Kusham, Rama Rao, P., Naganjaneyulu, K., 2023. The elusive crustal resistive boundary beneath the Deccan Volcanic Province and the western Dharwar craton, India. Geolog. Acta 21 (2), 1–14.

PROCMT User' guide, 1990. Offline processing software for magnetotelluric time series, Ver. 1.1. Metronix 75.

Prodehl, C., Kennett, B., Artemieva, I.M., Thybo, H., 2013. 100 years of seismic research on the Moho. Tectonophysics 609, 9–44.

Radhakrishna, B.P., Naqvi, S.M., 1986. Precambrian continental crust of India and its evolution. J. Geol. 94, 261–282.

Rajaram, M., Anand, S.P., 2014. Aeromagnetic signatures of Precambrian shield and suture zones of Peninsular India. Geosci. Front. 5, 3–15. doi:10.1016/j.gsf.2013.06.005.

Rajaram, M., Anand, S.P., Erram, V.C., Shinde, B.N., 2016. Insight into the structures below the Deccan trap-covered region of Maharashtra, India from geopotential data. Geol. Soc. Lond. Spec. Public. 445, 219–236. doi:10.1144/SP445.8.

Ramadass, G., Himabindu, D., Ramaprasada Rao, I.B., 2004. Magnetic basement

along the Jadcharla-Vasco transect, Dharwar Craton, India. Curr. Sci. 86, 1548–1553.

Raval, 1999. Some recent geophysical constraints from the central Gondwanaland. Pinsa 65 (3), 209–260.

Reynard, B., Mibe, K., Van de Moortele, B., 2011. Electrical conductivity of the serpentinised mantle and fluid flow in subduction zones. Earth Planet. Sci. Lett. 307, 387–394. doi:10.1016/j.epsl.2011.05.013.

Rice, J.R., 1992. Fault stress states, pore pressure distributions and the weakness of the San Andreas fault. In: Evans, B., Wong, T.-F. (Eds.), Fault Mechanics and Transport Properties of Rocks. Academic Press, New York, pp. 475–503.

Roberts, J.J., Tyburczy, J.A., 1999. Partial melt electrical conductivity: influence of melt composition. J. Geophys. Res. 104, 7055–7065.

Rodi, W., Mackie, R.L., 2001. Nonlinear conjugate gradients algorithm for 2-D magnetotelluric inversion. Geophysics 66, 174–187.

Rogers, J.J.W., Santosh, M., 2002. Configuration of Columbia, a Mesoproterozoic supercontinent. Gondwana Res. 5, 5–22.

Rogers, J.J.W., Santosh, M., 2004. Continents and Supercontinents. Oxford University Press, New York.

Rogers, J.J.W., Santosh, M., 2009. Tectonics and surface effects of the supercontinent Columbia. Gondwana Res. 15, 373–380.

Rogers, A.J., Kolb, J., Meyer, F.M., Armstrong, R.A., 2007. Tectono-magmatic evolution of the Hutti-Maski Greenstone Belt, India: constrained using geochemical and geochronological data. J. Asian Earth Sci. 31, 55–70.

Roy, S., Rao, R.U.M., 2000. Heat flow in the Indian shield. J. Geophys. Res. 105 (B11), 25587–25604.

Saha, D., Patranabis-Deb, S., Collins, A., 2016. Proterozoic stratigraphy of southern India cratons and global context. In: Stratigraphy & Timescales, 1. Elsevier Inc, pp. 1–59. doi:10.1016/bs.sats.2016.10.003.

Sarkar, D., Kumar, M.R., Saul, J., Kind, R., Raju, P.S., Chadha, R.K., Shukla, A.K., 2003. A receiver function perspective of the Dharwar craton (India) crustal structure. Geophys. J. Int. 154, 205–211. doi:10.1046/j.1365-246X.2003.01970.x.

Santosh, M., Hari, K.R., He, X.F., Han, Y.S., Manu Prasanth, M.P., 2018. Oldest lamproites from Peninsular India track the onset of Paleoproterozoic plumeinduced rifting and the birth of Large Igneous Province. Gondwana Res. 55, 1–20.

Santos, F.A.M., Mateus, A., Almeida, E.P., Pous, J., Mendes-Victor, L.A., 2002. Are some of the deep crustal conductive features found in SW Iberia caused by graphite? Earth Planet. Sci. Lett. 201 (2), 353–367.

Santosh, M., Maruyama, S., Yamamoto, S., 2009. The making and breaking of supercontinents: some speculations based on superplumes, super downwelling and the role of tectosphere. Gondwana Res. 15, 324–341.

Selway, K., 2014. On the causes of electrical conductivity anomalies in tectonically stable lithosphere. Surv. Geophys. 35, 219–257. doi:10.1007/s10712-013-9235-1.

Sen, G., 2001. Generation of Deccan trap magmas. Proc. Indian Acad. Sci. (Earth Planet. Sci.) 110 (4), 409–431.

Shankland, T.J., 1975. Electrical conduction in rocks and minerals: parameters for interpretation. Phys. Earth Planet. Inter. 10, 209–219.

Shellnutt, J.G., Hari, K.R., Liao, A.C.Y., Denyszyn, S.W., Vishwakarma, N., 2018. A 1.88 Ga giant radiating mafic dyke swarm across southern India and Western Australia. Precambrian Res. 308, 58–74.

Shobhita, K., Srinivasan, S., Paul, A., Nagaraju, M., Kumar, K.S., Umamaheshwar, K., Maithani, P.B., 2011. Petromineragraphic study of Oolitic Pyrite in radioactive Quartz Arenite of Phonda group from Kallamwadi area, Kolhapur and Sindhudurg districts, Maharashtra. In: Symp. Recent advances in applied geochemistry: current status and future trends ISAG 2011, Abstract, p. 67.

Singh, A., Singh, C., Kennett, B.L.N., 2015. A review of crust and upper mantle structure beneath the Indian subcontinent. Tectonophysics 644-645, 1–21. doi:10.1016/j.tecto.2015.01.007.

Sridhar, M., Chaturvedi, A.K., Rai, A.K., 2014. Locating new uranium occurrence by integrated weighted analysis in Kaladgi Basin, Karnataka. J. Geol. Soc. India 84, 509–512.

Sridhar, M., Markandeyulu, A., Chaturvedi, A.K., 2017. Mapping subtrappean sediments and delineating structure with the aid of heliborne time domain electromagnetics: case study from Kaladgi Basin, Karnataka. J. Appl. Geophys. 136, 9–18. doi:10.1016/j.jappgeo.2016.10.024.

Sridhar, M., Markandeyulu, A., Chawla, A.S., Chaturvedi, A.K., 2018. Analyses of aeromagnetic data to delineate basement structures and reveal buried igneous bodies in Kaladgi Basin, Karnataka. J. Geol. Soc. India 91, 165–173. doi:10.1007/s12594-018-0830-0.

Taylor, P.N., Chadwick, B., Moorbath, S., Ramakrishnan, M., Viswanatha, M.N., 1984. Petrography, chemistry and isotopic ages of Peninsular Gneisses, Dharwar acid volcanics and Chitradurga granites with special reference to Archaean evolution of Karnataka craton, Southern India. Precambrian Res. 23 (3–4), 349–375.

ten Grotenhuis, S.M., Drury, M.R., Peach, C.J., Spiers, C.J., 2004. Electrical properties of fine-grained olivine: evidence for grain boundary transport. J. Geophys. Res. 109, B06203. doi:10.1029/2003JB002799.

Tewari, H.C., Dixit, M.M., Sarkar, D., Kaila, K.L., 1991. A crustal density model across Cambay Basin, India and its relationship with the Aravalli. Tectonophysics 194, 123–130.

Tyburczy, J.A., Waff, H.S., 1983. Electrical conductivity of molten basalt and andesite to 25 kgbars pressure: geophysical significance and implications for charge transport and melt structure. J. Geophys. Res. 88 (B3), 2413–2430.

Vasanthi, A., Mallick, K., 2006. Bouguer gravity modeling of Kaladgi-Badami Basin, Karnataka. J. Geol. Soc. India 68, 937–945.

Vasanthi, A., Santosh, M., 2021. Lithospheric architecture and geodynamics of the Archean Dharwar craton and surrounding terranes: new insights from satellite gravity investigation. Gondwana Res. 95, 14–28.

Waff, H.S., Weill, D.F., 1975. Electrical conductivity of magmatic liquids effects of temperature, oxygen fugacity and composition. Earth Planet. Sci. Lett. 28, 254–260.

Wang, D., Guo, Y., Yu, Y., Karato, S., 2012. Electrical conductivity of amphibole-bearing rocks: influence of dehydration. Contrib. Mineral Petrol. 164, 17–25.

Wannamaker, P.E., Hasterok, D.P., Johnston, J.M., Stodt, J.A., Hall, D.B., Sodergren, T.L., Pellerin, L., Maris, V., Doerner, W.M., Groenewold, K.A., Unsworth, M.J., 2008. Lithospheric dismemberment and magmatic processes of the Great Basin Colorado Plateau transition, Utah, implied from magnetotellurics. Geochem. Geophys. Geosyst. 9 (5), Q05019. doi:10.1029/2007GC001886.

Watson, H.C., Roberts, J.J., Tyburczy, J.A., 2010. Effect of conductive impurities on electrical conductivity in polycrystalline olivine. Geophys. Res. Lett. 37 (L02302). doi:10.1029/2009GL041566.

Workman, R.K., Hauri, E., Hart, S.R., Wang, J., Blusztajn, J., 2006. Volatile and trace elements in basaltic glasses from Samoa: implications for water distribution in the mantle. Earth Planet. Sci. Lett. 241 (3), 932–951.

West, G.F., Edwards, R.N., 1985. A simple parametric model for the electromagnetic response of an anomalous body in a host medium. Geophysics 50, 2542–2559.

White, R., McKenzie, D., 1989. Magmatism at rift zones: the generation of volcanic continental margins and flood basalts. J. Geophys. Res. 94, 7685–7729.

Xu, Y., Shankland, T.J., Duba, A.G., 2000a. Pressure effect on electrical conductivity of mantle olivine. Phys. Earth Planet. Inter. 118, 149–161.

Xu, Y., Shankland, T.J., Poe, B.T., 2000b. Laboratory-based electrical conductivity in the Earth s mantle. J. Geophys. Res. 105 (B12), 27865–27875.

Yoshino, T., 2010. Laboratory Electrical Conductivity Measurement of Mantle Minerals. Surv. Geophys. 31, 163–206.

Yoshino, T., McIsaac, E., Laumonier, M., Katsura, T., 2012. Electrical conductivity of partial molten carbonate peridotite. Phys. Earth Planet. Inter. 194–195.

Zhao, D., 2001. Seismic structure and origin of hotspots and mantle plumes. Earth Planet. Sci. Lett. 192 (3), 251–265. doi:10.1016/s0012-821x(01)00465-4.